Masarykova univerzita
Přírodovědecká fakulta
Ústav fyzikální elektroniky

# Bakalářská práce

Brno 2019 Ivan Fiebig

Masarykova univerzita
Přírodovědecká fakulta
Ústav fyzikální elektroniky

# Elektrony iniciovaná chemie v mikroplazmatu na trojném rozhraní

Bakalářská práce

**Ivan Fiebig**

**Vedoucí práce: Mgr. Tomáš Hoder Ph.D.** **Brno 2019**

## Bibliografický záznam

| | |
|---|---|
| **Autor:** | Ivan Fiebig<br>Přírodovědecká fakulta, Masarykova univerzita<br>Ústav fyzikální elektroniky |
| **Název práce:** | Elektrony iniciovaná chemie v mikroplazmatu na trojném rozhraní |
| **Studijní program:** | Fyzika |
| **Obor:** | Fyzika |
| **Vedoucí práce:** | Mgr. Tomáš Hoder Ph.D. |
| **Akademický rok:** | 2018/2019 |
| **Počet stran:** | x + 58 |
| **Klíčová slova:** | elektrické pole, trojné rozhraní, bariérový výboj, plazmová chemie, ekvivalentní elektrický obvod |

## Bibliographic record

| | |
|---|---|
| **Author:** | Ivan Fiebig<br>Faculty of Science, Masaryk University<br>Department of physical electronics |
| **Title of Thesis:** | Electron initiated chemistry of microplasma at the triple junction |
| **Degree Programme:** | Physics |
| **Field of study:** | Physics |
| **Supervisor:** | Mgr. Tomáš Hoder Ph.D. |
| **Academic Year:** | 2018/2019 |
| **Number of Pages:** | x + 58 |
| **Keywords:** | electric field, triple junction, barrier discharge, plasma chemistry, equivalent electric circuit |

## Abstrakt

Cílem této práce je pokusit se dosáhnout dostatečně dobré aproximace elektrického pole ve výbojové komoře jenom pomocí analytického řešení použitých rovnic. Náš pokus bude vykonán metodou ekvivalentního obvodu. Obvod výbojové komory bude nahrazen ekvivalentním obvodem s odporovými a kapacitními elementy, elektrické pole pak vypočteno pomocí makroskopických veličin, které mohou být snadno naměřeny. Nás odhad pak bude porovnán s důvěryhodným spektroskopickým meřením. V případě prokázané použitelnosti bude následně použit s pomocí programu na výpočet Boltzmannovy kinetické rovnice k výpočtu reakčních a transportních koeficientů zkoumaných procesů. Naše pozornost bude zaměřena na bariérové výboje, nebo konkrétněji, povrchové bariérové výboje.

## Abstract

The goal of this thesis is to try to achieve good enough approximation of the electric field in a discharge cell only by analytically solving used equations. Our attempt will be executed via method of equivalent circuit. Circuit with a discharge cell will be replaced with an equivalent circuit with resistive and capacitive elements; electric field will be calcutated via macroscopic quantities, which can be easily measured. Our estimate will then be compared to a trusted spectroscopic measurement. If proven valid, it will then be used with Boltzmann equation solver to calculate rate and transport coefficients of the examined process. Our focus will be brought to dielectric barrier discharges (DBDs), or more precisely, surface DBDs.

MASARYKOVA UNIVERZITA
Přírodovědecká fakulta

# ZADÁNÍ BAKALÁŘSKÉ PRÁCE

Akademický rok: 2018/2019

**Ústav:** Ústav fyzikální elektroniky

**Student:** Ivan Fiebig

**Program:** Fyzika

**Obor:** Fyzika

Ředitel *Ústavu fyzikální elektroniky* PřF MU Vám ve smyslu Studijního a zkušebního řádu MU určuje bakalářskou práci s názvem:

**Název práce:** Elektrony iniciovaná chemie v mikroplazmatu na trojném rozhrani

**Název práce anglicky:** Electron initiated chemistry of microplasma at the triple junction

**Oficiální zadání:**
Mikroplazma generované za atmosferického tlaku na rozhraní různých materiálů je zdrojem vysokých gradientů elektrického pole či teploty. Mikroplazma funguje pak jako mikroskopický chemický reaktor, kde jsou chemické reakce řízeny elektrony urychlovanými v lokálních elektrických polích. Díky těmto vlastnostem je takové plazma využíváno v mnoha aplikacích (v generátorech ozónu, jako zdroje elektrického větru v leteckém inženýrství nebo jako mikroskopické trysky dávkující reaktivní chemické částice v biomedicínských aplikacích fyziky plazmatu). Náplní práce bude vyšetřit použitelnost přibližných modelů a konceptů ke kvantifikaci elektrického pole v plazmatu a poté určení reakčních koeficientů vybraných plazmochemických reakcí. Tyto informace pak poslouží k popsání elektrony iniciované chemie v mikroplazmatu, které je generováno v plynu na rozhraní vodní hladiny či kovu a dielektrického povrchu. Využije se aproximativních elektrických přístupů [1], spektroskopických metod s pikosekundovým rozlišením a vysokou citlivostí a analytického modelu [2] k popsání elektrického pole v plazmatu. Z řešení Boltzmannovy kinetické rovnice [3] budou získány reakční koeficienty pro popis plazmové chemie směsi použitého plynu a vodních par. [1] Pipa A V et al. 2012 Review of Scientific Instruments 83, 115112, [2] Wang Y et al. IEEE Plasma Sci. 44, 2796, [3] Hagelaar G J M et al. 2005 Plasma Sources Sci. Technol 14, 722-733.

**Jazyk závěrečné práce:** Anglický jazyk

**Vedoucí práce:** Mgr. Tomáš Hoder, Ph.D.

**Konzultant:** Mgr. Zdeněk Bonaventura, Ph.D.

**Datum zadání práce:** 19. 5. 2018

**V Brně dne:** 23. 4. 2019

Souhlasím se zadáním (podpis, datum):

| | | |
|---|---|---|
| ..... | ..... | ..... |
| Ivan Fiebig | Mgr. Tomáš Hoder, Ph.D. | prof. Mgr. Petr Vašina, Ph.D. |
| **student** | **vedoucí práce** | **ředitel Ústavu fyzikální elektroniky** |

## Poděkování

My biggest gratitude goes to my supervisor Mgr. Tomáš Hoder, Ph.D. for his endless patience, availability and willingness to provide answers to all of my questions. I also want to thank Mgr. Lukáš Kusýn and Mgr. Petr Synek, Ph.D. for providing experimental data analyzed in this thesis. My gratitude also belongs to my parents for both moral and financial support in my studies.

## Prohlášení

Prohlašuji, že jsem svoji bakalářskou práci vypracoval samostatně s využitím informačních zdrojů, které jsou v práci citovány.

Brno, 23. května 2019

Podpis autora

# Contents

**Introduction** **1**

**1 Dielectric barrier discharges** **3**
1.1 *Basic configurations* . . . . . 4
1.2 *Mechanisms* . . . . . 5
1.2.1 Avalanche and streamer formation . . . . . 5
1.2.2 Discharge properties . . . . . 9
1.3 *Optical emission spectroscopy* . . . . . 11
1.4 *Equivalent circuits* . . . . . 14
1.4.1 Simplest circuit . . . . . 14
1.4.2 Alternative equivalent circuit . . . . . 17
1.5 *Calculations of plasma driven chemistry* . . . . . 19

**2 Experimental setup** **23**

**3 Theoretical clarifications of measured quantities** **25**
3.1 *Simplest equivalent circuit* . . . . . 25
3.2 *Alternative equivalent circuit* . . . . . 28
3.3 *Capacitances* . . . . . 31
3.4 *Electric field* . . . . . 32

**4 Results and discussion** **33**
4.1 *Fused silica tube configuration* . . . . . 33
4.2 *Radially symmetrical setup in humid air* . . . . . 37
4.3 *Rate and transport coefficient analysis* . . . . . 47

**5 Conclusion and outlook** **53**

# Introduction

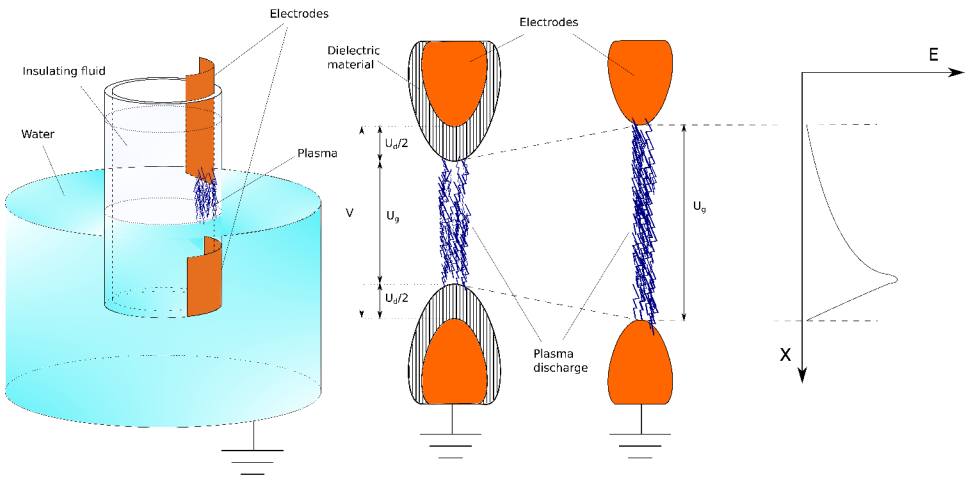


Figure 1: On the left–actual configuration of an experiment. In the middle are shown consecutive approximations. On the right–graph of field intensity distribution $E(x)$ in gas gap.

In many industrial areas where plasma is used, spatial and time distributions of the electric field during a discharge are wanted. Its value is an important parameter in calculation of various rate coefficients of chemical reactions, which are in most part initiated by electrons. Thus, knowledge of $E$ is essential for optimizing industrial processes, be it for economic reasons, need for achieving certain efficiency or protection of processed material (e.g. protecting life of seeds in disinfication process). Determination of electric field function is often a very complex and time-consuming task. It includes precise scan of used electrodes and various simulations for the concrete setup, or complex experimental methods.

The ambition of this thesis is achieving good enough approximation of the electric field function only by analyticaly solving used equations. If such a feature can be achieved for certain configurations, the results could be used for faster and easier calculations of $E$. Method of equivalent circuit will be tried for fulfilling this goal. It will be described for volume discharge and with slight adjustment applied for surface discharge. Method of equivalent circuit in the end works only with macroscopic quantities like capacitance and resistance, disregarding shape of the electrodes. Approximation process is shown on figure 1. The initial experiment examined in this thesis is

composed of two electrodes, one placed on the inner, and the other placed on the outer side of a glass tube. Discharging occurs on outer surface on the tube. Equivalent circuit will provide the ability to express voltage in the discharge area $U_g$ in terms of applied voltage and current (chapter 3) and "get rid" of the dielectric barriers. With the help of spectroscopic measurement provided and an electric field distribution function approximation developed in [1], maximum value of $E$ will be estimated. This value will then serve as input to BOLSIG+ Boltzmann equation solver to obtain wanted rate coefficients of chosen chemical reactions.

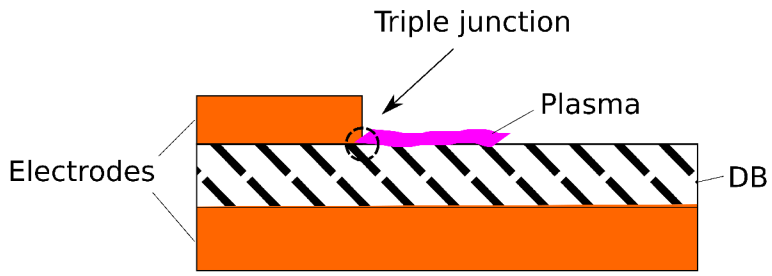


Figure 2: Sketched surface barrier discharge. Triple junction location marked out.

A point where 3 different electrical mediums meet is called triple junction. A very high eletric field is generated around this junction, thus it is often the point where discharges are initiated. Its location is marked on sketched figure 2. It has been researched for example for its possible use in surface treatment [2], and also for its negative effect of insulator flashovers [3].

# 1 Dielectric barrier discharges

Dielectric barrier discharges (DBDs), also called silent discharges, ozonizer discharges or just barrier discharges, are self-sustaining discharges in such configurations, that one (or both) electrode is separated from the other by a dielectric material (quartz, ceramic, teflon, plastics, silicon rubber etc.) [4]. During the discharge, charged particles are accumulated on the surface of the dielectric, causing the discharge to quench, thus creating a self-pulsing operation. Therefore, DBD cannot be sustained by a continuous DC voltage. Either AC voltage or pulsing DC voltage shall be applied. DBDs are a non-thermal, non-equilibrium discharges operating at atmospheric pressure. Charge carriers present in DBD are mostly created by dielectric breakdown of the gas between electrodes. Despite low temperature, electrons present have high mean energy, which makes them very effective in generating radicals and activated species, and thus inducing various chemical reactions. These properties makes them usable in a broad range of applications, such as surface treatment, disinfection of seeds in agriculture, biomedical applications and collection of submicrometre particles from the air. The most widely used application is the generation of ozone, for which they were first introduced [5].

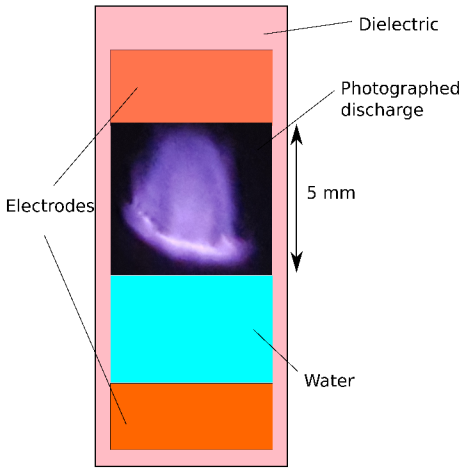


Figure 1.1: Example of a DBD. Photograph was taken during a conducted experiment.

## 1.1 Basic configurations

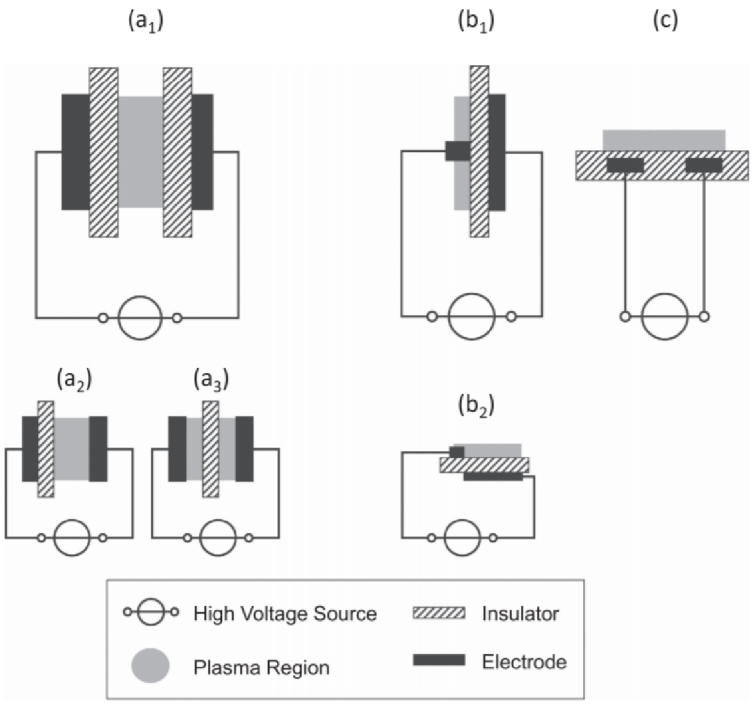


Figure 1.2: Basic configurations of DBDs: ($a_1$–$a_3$) volume DBD (1–symmetric, 2–asymmetric, 3–floated dielectric), ($b_1$–$b_2$) surface DBD (1–symmetric, 2–asymmetric), (c) coplanar discharge. Taken from [4].

Cell of a DBD is typically composed of two electrodes, at least one dielectric barrier between them and also a gas gap, either in between the electrodes, or alongside the surface of the dieletric (surface discharges). Most often used gases are rare gases, nitrogen, oxygen and mixtures of these gases. Length of the discharge gap is usually 0,1–10 mm. Usual voltages used are 1–100 kV [4].

By the configuration of discharge cell, different types of DBDs are recognized. Some basic ones are depicted on figure 1.2. In so called volume dielectric barrier discharges or volume barrier discharges (VBD), the discharge burns in between the electrodes. Such configurations are depicted on ($a_1$)–($a_3$). In ($a_1$), the discharge needs to be operated at higher voltage than in ($a_2$) and ($a_3$), as there are two dielectrics. Hence the smaller fraction of the applied voltage drops over the gas gap area. However, this configuration has

an advantage of both electrodes being covered, thus protected from erosion caused by the plasma.

In surface discharges or SBDs ((b$_1$)–(b$_2$)) both electrodes are in contact with the dielectric and the discharge burns alongside its surface. One of the electrodes is usually embedded completely in dielectric, so that discharge occurs only around one of the electrodes. Focus of this thesis will be brought mainly on this type of configuration.

Type of discharge shown in (c) is called coplanar discharge. In this arrangement, both electrodes are embedded in the dielectric barrier and the discharge occurs on the surface of one side of the barrier [6].

## 1.2 Mechanisms

### 1.2.1 Avalanche and streamer formation

DBDs have a characteristics of a streamer. With a naked eye, one sees them as thin filamentary discharges. Each filament is however composed of many streamer channels also called microdischarges. Individual microdischarges are more or less equivalent, thus description of only one of them is satisfactory. Mechanism of streamer type of discharge will be briefly discribed in this section. It can be divided into three phases: townsend phase (pre-breakdown), streamer propagation phase and the decay phase [7].

When a certain voltage on the electrodes is reached (breakdown voltage), an avalanche event is initiated near the surface of cathode. For simplicity, let the avalanche be initiated by a single electron emitted from the cathode. It is accelerated by the applied field $\vec{E}_0$ on the electrodes. The electron then excites another electron from the dielectric and the process repeats, creating a chain reaction. In AC driven discharges, discharge is almost always initiated by many electrons stored on the dielectric surface from previous discharge. Newly created electrons are pulled towards anode by the field $\vec{E}_0$. Propagating electrons are however diffused radially, and the front part of the avalanche takes form of a spherical "head". Electron and ion concentrations obey general diffuson equation:

$$\frac{\partial n}{\partial t} + \mathrm{div}\Gamma = q, \tag{1.1}$$

where $n$ is concentration of particles, $\Gamma$ is flux of the particles and $q$ represents bulk sources of creation a anihilation of particles. The solution for electron concentration $n_e$ takes form of :

$$n_e = (4\pi D_e t)^{-3/2} \cdot \exp\left(-\frac{(x - v_d t)^2 + r^2}{4D_e t} + (\alpha - a)^2\right). \quad [8] \tag{1.2}$$

Here $D_e$ is the diffusion coeficient, $t$ is time passed from the start of an avalanche, $x$ is the distance from the cathode, $r$ is radial distance from the x-axis, $v_d$ drift velocity of the central point of the avalanche, $\alpha$ ionization and $a$ attachment coeficients. We see that $n_e$ decreases with distance from the central point of the avalanche following the Gaussian law.

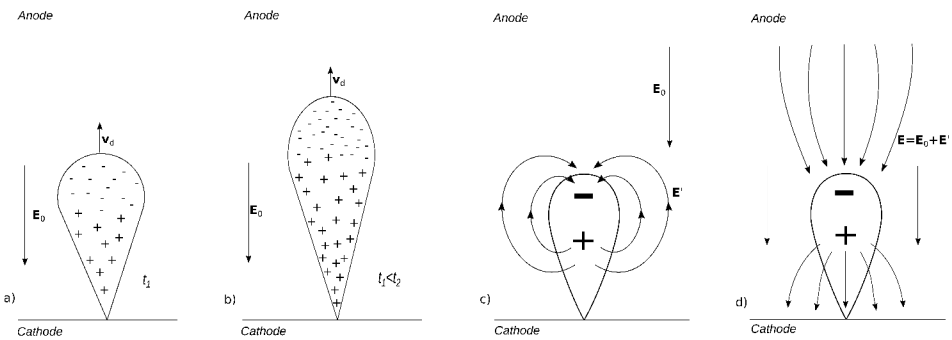


Figure 1.3: Demonstrative figure of avalanche propagation. a) Electron avalanche moving towards anode, leaving positive ions behind. $\vec{E_0}$ is the applied external voltage. b) Same electron avalanche in latter time $t_2 > t_1$. c) Field induced by volume charges. d) Overall field in the gap. Reconstructed from [8].

As electrons move towards anode, they leave behind large amount of positive ions which leads into formation of another field $\vec{E'}$ with a dipole character. Propagation of an avalanche is depicted on figure 1.3. An avalanche will transform into so called streamer, when a certain condition is met. The streamer is formed when value of $\vec{E'}$ reaches order of magnitude of $\vec{E_0}$.

$$\vec{E'} = eR^{-2} \exp(\alpha(E_0)x) \approx E_0 \quad [8] \tag{1.3}$$

Then the overall field $\vec{E} = \vec{E_0} + \vec{E'}$ is approximately zero and a quasineutral plasma is formed. This quasineutral thin channel is very condutive and can lead into high current transfer once it reaches the electrodes. This condition for a streamer formation was first used by Loeb and Meek. $R$ represents radius of the avalanche head and $x$ is some point on the axis perpendicular to

the electrode planes. For a streamer to form, this condition must be met for $x$ less or equal to the distance between electrodes.

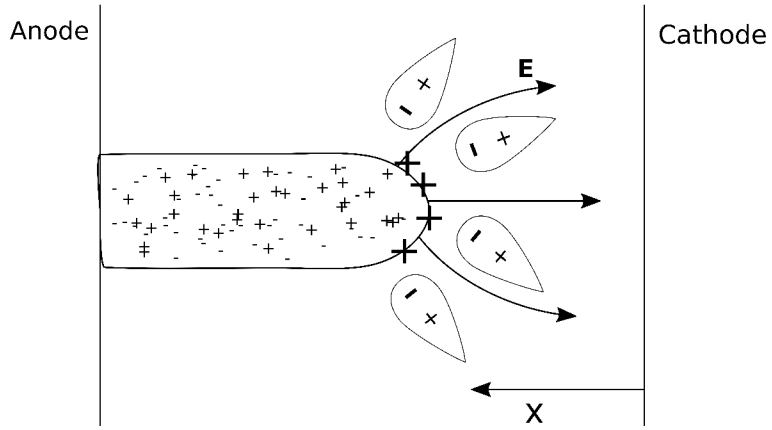


Figure 1.4: Streamer propagation. Quasineutral channel propagates towards cathode. Secondary avalanches are pulled in by streamer head positively charged from ions left behind by previous generation of avalanches. Reconstructed from [9].

In not too wide gaps and not too high fields $\vec{E}_0$ this criterion is usually met when avalanche reaches the anode. Streamer will start to form at the point of maximum space charge, that is, at close vicinity of the anode surface. It will then grow towards the cathode and, it is therefore called cathode-directed or positive streamer (fig. 1.4). Required amount of space charge can be reached even earlier if applied voltage is significantly higher than breakdown voltage of the dielectric or when gap is sufficiently wide. Streamer then grows towards both of the electrodes. In case that streamer is formed relatively close to the surface of cathode, it grows mostly towards anode and is therefore called anode-directed or negative.

It is thought that grow of a streamer is caused by photons created by recombination in excited atoms in the avalanche. In cathode-directed growth, these photons excite surrounding atoms and form secondary avalanches, which grow towards the primary avalanche. When they reach its path, electrons from the secondary avalanches will generate a quasineutral plasma with ions from the primary avalanche and will create more photons which initiate next generation of secondary avalanches. Positive ions from the first generation will then stir second generation of avalanches towards them and

the process repeats. In anode-directed growth, the mechanism is slightly different. Electrons in secondary avalanches are repelled by negatively charged head of the primary avalanche. They leave a trail of positive ions behind them and the electrons of the primary avalanche are dragged into them in contrast to cathode-directed growth.

The streamer phase is the one that will concern us, when it comes to electric field approximation. Most of $E_0$ distortion happens in close vicinity of streamer head. This head is in [1] approximated by sphere (radius $R$), so that tip of a streamer head coincides with a point on spheres surface. If we place zero point of x coordinate in fig. 1.4 to the center of streamer head, sphere region will coincide with positively charged region of the head. Field is in [1] approximated linearly in this region and inversely to x coordinate after zero point as follows:

$$E(x) = \begin{cases} E_{max}\left(1 - \frac{x}{R}\right), & 0 \leq x \leq R, \\ \dfrac{E_{max}}{1 - \frac{x}{2R}} & x \leq 0. \end{cases}$$

After streamer connects the electrodes, charge is transferred through the streamer channel and deposited on the surface of DB(s). This deposited charge induces a field which hinders more discharge activity unless voltage is risen or its polarity switched. This phase is known as the decay phase. It schould be noted that, unless there is enough time between individual voltage pulses in pulsing mode operation for the accumulated charge to dissipate, it will affect next discharge phase. Discharges will be less likely to occur between the locations with accumulated charge as it will induce electric field of the opposite polarity to the applied voltage. Deposited charges can also travel throughout the surface of the dielectrics, which may cause need for higher applied voltage and prolong townsend phase if their distribution becomes homogenous enough. In AC operation mode, lower voltage will be needed for the avalanche creation, and they will more likely occur in the same location as in previous half-cycle.

### 1.2.2 Discharge properties

**Volume barrier discharge.** Temporal length and structure of discharge channels depend on type of used electrodes (whether they are dielectricaly covered or not). In [10], an optical measurement revealed that if anode is conductive (uncovered), channel duration will be significantly longer. This can be explained by the fact that if anode is covered, electrons will accumulate of the dielectric barrier, thus screening intensity of the applied field and quenching the discharge in the channel. Moreover, if one of the electrodes is non-conductive, accumulated charge will spread along the dielectric surface, blocking the ability of other seperate streamers to form in close vicinity to the first one.

**Coplanar barrier discharges.** Coplanar discharge is composed of several parallel microdischarges extending to the points on dielectric surface above electrode tips. Channels influence formation of successive channels by charge accumulation on dielectric surface (this is also true for other DBD types). In the initial phase of the discharge, value of component of electric field parallel to the connecting line of electrodes is the highest in the middle between electrodes. This means the forming channel will be higher in the middle of the discharge path. Perpendicular coponent has the highest positive value at the anode, while at the cathode the component has the highest negative value. Later on, as discharge channels develop from cathode and anode directed streamers, charge will be accumulated on both sides leaving the middle region with basically zero field strength. Even after extinction of the channels, some charge remains near the electrode positions which alters conditions for the next discharge.

**Surface barrier discharges.** In surface discharge configurations, one electrode is above surface of a dielectric and the other, much wider electrode is positioned under it. Discharge occurs on the dielectric surface from the conductive electrode to some distance from it, determined only by amplitude of the applied voltage. This is in constast to symmetric VDB and CDB discharges, where the discharge region is limited by the position of electrodes. For a single voltage pulse, charge is deposited on the dielectric surface during the voltage rise. Later, as voltage decreases, accumulated charge causes so called backward discharge of the opposite direction, reducing the amount of charge accumulated. However, covered area is much smaller than that of the previous discharge, so the amount of charge is unchanged from a cer-

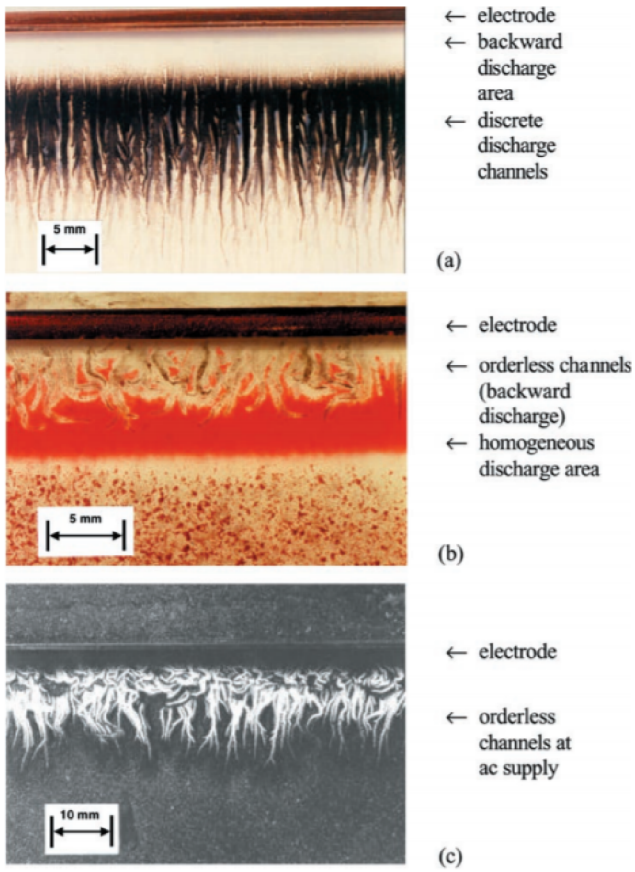


Figure 1.5: Discharge patterns of an SBD arrangement: (a) a positive voltage pulse of 20 kV, (b) a negative voltage pulse of 20 kV, (c) an AC voltage of 10 kV. Taken from [11].

tain distance from the electrode [11]. Charged area is larger when sucessive positive pulses are used, compared to sucessive negative pulses. If AC voltage is used, the size of charged area is somewhere in between. Length of the discharge patterns is except voltage, determined by the permitivity od used dielectric material. The higher the permitivity, the shorter discharge paths will be observed.

Initial phase of SBD arrangement is different than that od VBD. Initial field strength distribution is not uniform and only in short distance from the cathode multiplication coefficient is positive. Multiplying electrons move away from the cathode along DB surface to the region of excessive attach-

ment processes, where their number is reduced. However, they emit photons causing photoionization on the cathode, creating secondary avalanches. Later on, amount of charge on the DB surface reaches saturation level and charge accumulation is only possible at larger distances from the cathode. Electrons then move in a thin layer above the dielectric surface, and are deposited on the far end on the discharge path.

In [12], modeling of SBD in air revealed that discharge current has different development for positive (dielectrically covered cathode) and negative (dielectrically covered anode) applied voltages. In positive polarity, discharge current spikes appeared with lower frequency and higher amplitude than in negative polarity. In negative polarity, 10 times higher frequency and 10 times lower amplitude were observed. Also, current did not return to original value after spike occurence, but instead minimal current slightly increased with each current spike during the voltage rise, which suggests presence of some coninuous current flow. Based on these results, different current profiles of positive and negative sinusoidal voltage half-periods can be expected for our experiments. This effect can be damped by raising permitivity of the dielectric. Dielectric with high permitivity is closer to conductor, which can be thought of as dielectric with infinite permitivity. The asymmetry of the setup will then disappear. Different current developments are also present in asymmetric VBDs [10].

## 1.3 Optical emission spectroscopy

On figure 1.6 is depicted a typical spectral characteristics of a surface DBD. It mainly consists of the spectrum of second positive system of molecular nitrogen (SPS) and usually one visible transition 0-0 of first negative system of molecular nitrogen (FNS). We will later be concerned about 0-0 transition of SPS ($\lambda = 337,1$ nm). This transition occurs as a result of the following process:

$$\mathrm{e^{+}N_2(X^1\,\Sigma_g{}^{+})_{\nu=0} \rightarrow N_2(C^3\Pi_u)_{\nu'=0} + e\ (E{=}11\ eV)} \tag{1.4}$$

$$\mathrm{N_2(C^3\Pi_u)_{\nu'=0} \rightarrow N_2(B^3\Pi_g)_{\nu''=0} + h\nu}\ . \tag{1.5}$$

DBDs are very short duration pulses which often lasts only a few nanoseconds due to their streamer nature. Cross-correlation spectroscopy (CCS) is a method used to measure very fast light pulses, making it very suitable for DBD observations. Instead of measuring luminosity from a single pulse, a

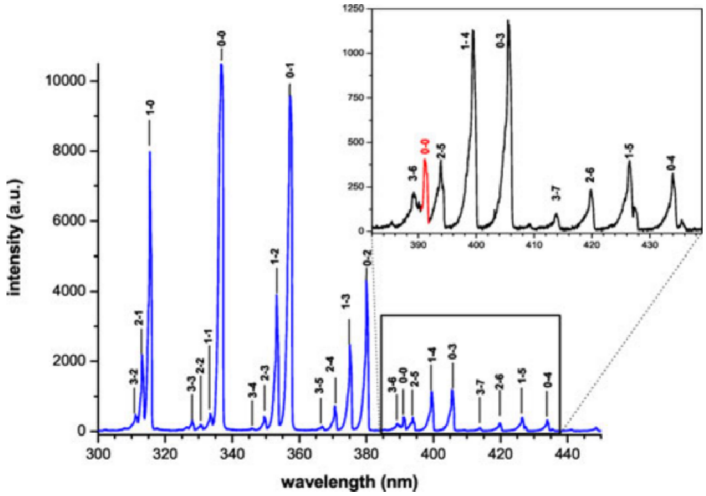


Figure 1.6: Typical spectrum of DBD at atmospheric pressure air. Spectral bands in blue mark SPS, red marked spectral band in zoomed spectrum is FNS. Taken from [13].

repetitive pulse is used and the profile of the light pulse is calculated statistically. In contrary to classical spectroscopy, it can measure spatio-temporary distribution of the signal with sub-nanosecond resolution. Two signals are needed: the synchronizing signal, which provides a relative time scale, and the main signal. These signals have to originate from the same source and the main signal needs to be measured with probability at least 1 order of magnitude lower than that of the synchronizing signal. The measured quantity in this method is time delay between the signals and the record ed quantity is a probability density function for the evolution of the light pulse intensity.

In [14], CCS was used to measure spatial-temporary distribution of luminosity of volume DBD in air at atmospheric pressure. Figure 1.7 shows experimental setup used. The main signal is spatially and spectrally resolved. It consist of a single photon, later multiplicated in photomultiplier. As main signal enters the so called time correlated single photon counting module (TCSPCM), it triggers a time measurement which stops when synchronizing signal enters the TCSPCM. Synchronizing signal must be delayed by a coaxial cable in order to be able to measure photons coming from second half of the pulse as the trigger is set to maximum of the pulse. From known time delay between the two signals, recorded photon can be placed in time

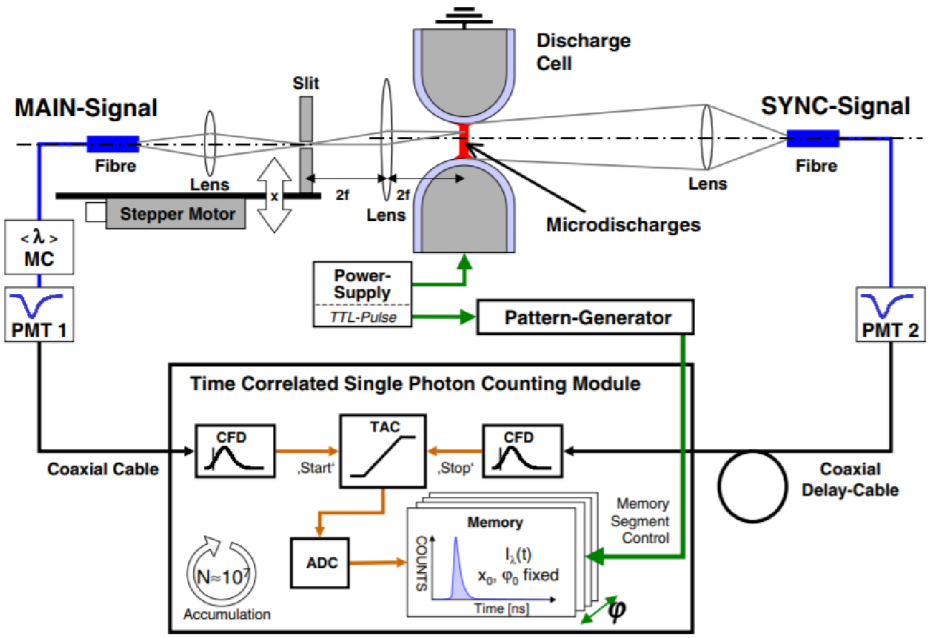


Figure 1.7: Diagram of the apparatus and measurement procedure: MC–monochromator, PMT–photomultiplier, TTL–transistor–transistor logic, CFD–constant fraction discriminator, TAC–time-to-amplitude converter, ADC–analogue-to-digital converter, $\varphi$–phase of the applied sinusoidal voltage. Taken from [14].

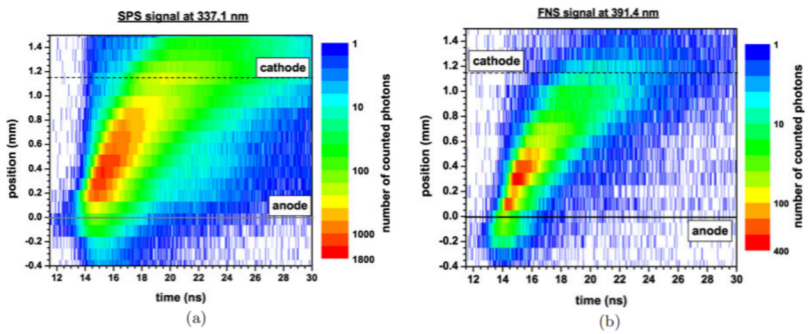


Figure 1.8: Development of intensities of 0-0 transitions of (a) SPS (337,1 nm) and (b) FNS (391,5 nm) of nitrogen. Dashed line depicts the covered electrode. Taken from [13].

scale. By measuring one-photon pulses many times, a time dependent intensity profile of the pulse can be generated by counting photons with the same time delay. This delay can be measured in order of tens of ps. SPS and FNS spatio-temporal distribution of luminosities for positive voltage half-period is shown on figure 1.8. It was measured in [13] for SBD arrangement.

## 1.4 Equivalent circuits

Goal of this thesis is to estimate field $E$ only from precise measurement of macroscopic quantities, that is, without numerical simulations of space temporal particle distribution. For this, a model of equivalent circuit shall be used. Discharge cell consists of conductive electrodes, dielectric barrier and gas gap. DB and the gas gap have certain capacities, latter one changes when discharge is ignited. During the discharge, gas gap also contains resistive element because of non-zero current flowing through it. Both capacitive and resistive attributes of the gas gap must be accounted for. If one will treat the gap as a simple resistor, capacitance of discharge cell would change for no reason at the moment of discharge ignition. If only capacitive character will be considered, it would not describe non-zero voltage in the gas gap.

### 1.4.1 Simplest circuit

For simplest equivalent circuit, theory applied by Pipa et al. will be considered [15][16]. Notation used in referenced documents will be retained. The simplest equivalent circuit is sketched on figure 1.9. Charges accumulated on plates of capacitors $C_d$ and $C_g$ connected by the internal node is equal to the charge transferred through resistor $R$. From this scheme, following equation can be written.

$$Q(t) = C_d(V(t) \pm U_g) \tag{1.6}$$

Here gap voltage $U_g$ is considered a positive quantity, because only its absolute value matters in reduced field $E/N$ determination. At the end of a discharge, charge $\pm q_{max}/2$ will be accumulated on the $C_d$ and $C_g$ capacitors. Its sign depends on polarity of the applied voltage. This means that during one half cycle of sinusoidally changing $V(t)$ (one discharge phase), charge $q_{max}$ will be transferred. In the dark phase (without discharge), resistance $R$ is infinite. The overall capacitance od the cell $C_{cell}$ can then be expressed as capacity of the DB $C_d$ and capacity of the gas gap $C_g$ connected is series,

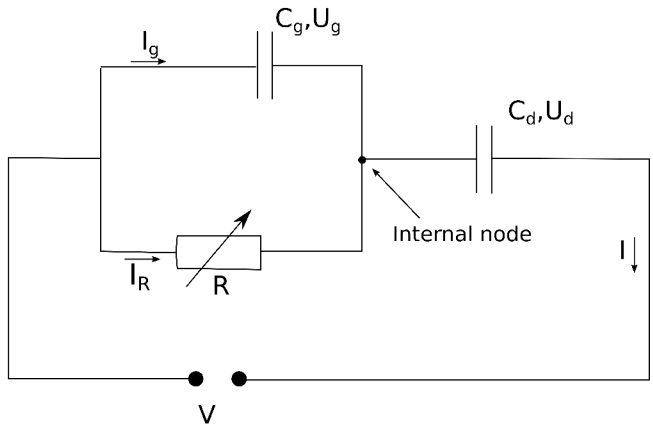


Figure 1.9: Simplest equivalent circuit. Reconstructed from[15].

therefore:

$$C_{cell} = \frac{C_g C_d}{C_g + C_d}. \tag{1.7}$$

Let us now write a charge accumulated on individual capacitors after one discharge. Because they feel the same voltage, charge will be distributed on them by the ratio of their capacities.

$$\tilde{q_g} = \frac{C_{cell}}{C_d} \frac{q_{max}}{2}, \tag{1.8}$$

$$\tilde{q_d} = \left(1 - \frac{C_{cell}}{C_d}\right) \frac{q_{max}}{2}. \tag{1.9}$$

Charge value after discharge depends only on applied voltage, therefore, it can be expressed in the arbitrary point in the dark phase as:

$$q_d = C_{cell} V(t) \pm \tilde{q_d}. \tag{1.10}$$

Equation (1.10) may be rewritten into:

$$Q(t) \pm \frac{Q_0}{2} = C_{cell} V(t). \tag{1.11}$$

Here $Q(t) = q_d$ and $\frac{Q_0}{2} = \tilde{q_d}$. From equations (1.6) and (1.11) a Q-V plot may be constructed for charge deposited on the dielectric barrier. This is the charge that can actually be measured by integrating current flowing through the discharge cell circuit. It will take form of a parallelogram, depicted on figure 1.10. Capacitances $C_d$ and $C_{cell}$ can be determined as slopes of parallelograms sides.

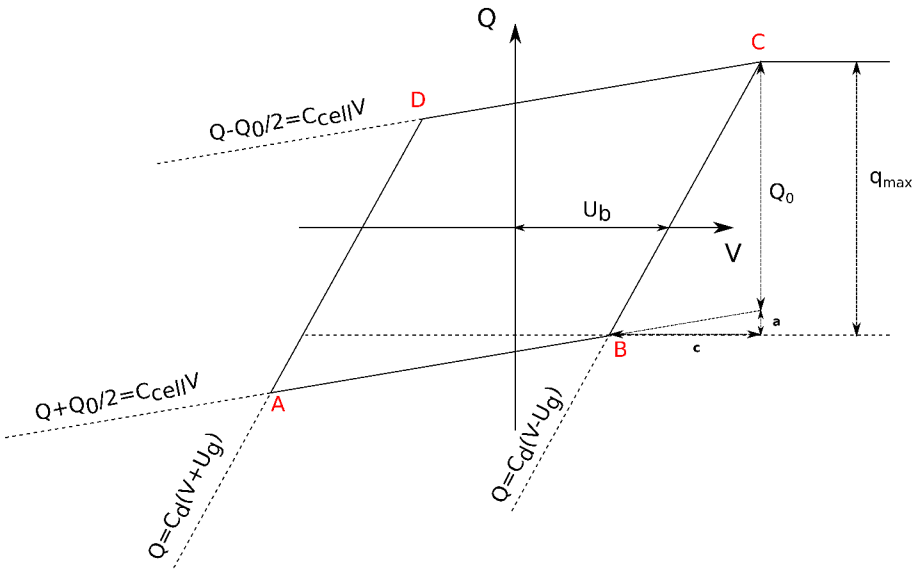


Figure 1.10: Q–V plot for the simplest equivalent circuit. Shape corresponds to the classical sinusoidal voltage driven ozonizer. Sides AB and CD correspond to the dark phases. Sides BC and DA correspond to the discharge phases Reconstructed from [15].

It has been stated that $q_{max}$ corresponds to the variation of charge during one discharge. $Q_0$ corresponds to the charge variation on the DB. Relation between these two quantities can be derived from the parallelogram. Their difference is clearly segment "a" in figure 1.9. Slope of the sides AD and BC is $C_d$ and slope of sides AB and CD is $C_{cell}$. Taking this into account following relations can easily be obtained.

$$\frac{q_{max}}{c} = C_d \tag{1.12}$$

$$\frac{q_{max} - Q_0}{c} = C_{cell} \tag{1.13}$$

By eliminating "c" from the equations, wanted relation is obtained.

$$Q_0 = \left(1 - \frac{C_{cell}}{C_d}\right) q_{max} \tag{1.14}$$

Quantity $U_b$ depicted on figure 1.10 represents effective breakdown voltage of the gas gap. Word effective is used because voltage needed for discharge to start is lower than breakdown voltage of gas in the gap (due to charge accumulation on DB). At the point of the discharge beginning (B, D), $U_g$ clearly

has to have value of $U_b$. Model of simplest equivalent circuit assumes that $U_g$ remains constant through the whole discharge phase. Thus, resulting from the equation (1.6), $V(t) = U_g = U_b$ at zero transfered charge $Q(t)$.

It schould be noted that in reality $U_g$ is not constant during discharge phase, but instead changes with changing applied voltage $V(t)$ and decreases with each microdischarge due to resistive loses in the gas gap. Observations of decrease in gap voltage implicate presence of several microdischarges. Parallelogram shape will be observed for large setups where charge transferred through one microdischarge is insignificant. In small laboratory setups like ours, a stair like function will be observed between points B,C and D,A. Additionally, $U_g$ is not homogenous throughout capacitor plates as the discharge is also not homogenous. $U_g$ used therefore represents only an effective value. Implications of these facts will be discussed later.

### 1.4.2 Alternative equivalent circuit

As was already mentioned, DBDs are not homogenous, but instead have a filamentary character. Therefore, part of the electrode surface will be discharged and part will not. Simplest equivalent circuit counts with whole surface discharging. This can be corrected by adding a parallel branch to the circuit, in which resistance $R$ is absent. This alternative circuit was developed by Peeters and van de Sanden in [17]. Notation for capacitances and voltages will be retained from this work.

Alternative equivalent circuit is depicted on figure 1.11. Charges $q_{cell}$ accumulated on non-discharging branch, $q_{diel}$ accumulated on dielectric in discharging branch and $q_{gap}$ accumulated on capacity of the discharging part of the gap are defined as follows:

$$q_{cell}(t) = \alpha C_{cell} V(t), \tag{1.15}$$

$$q_{diel}(t) = \beta C_{diel} U_{diel}(t), \tag{1.16}$$

$$q_{gap}(t) = \beta C_{gap} U_{gap}(t). \tag{1.17}$$

$\alpha$ and $\beta$ coefficients define fractions of the elecrode surface in which charge is or is not present, respectively. Clearly $\alpha + \beta = 1$. It schould be also noted that $U_{gap}$, although equivalent with $U_g$ from previous section, is defined only for $\beta$ branch (discharging branch). On figure 1.12 there are two parallelograms, (a) depicting circuit with $\beta = 1$, $\alpha = 0$ and (b) depicting circuit with arbitrary $\beta$, $\alpha$. In case (a), Q-V plot is basically equivalent to that of simplest

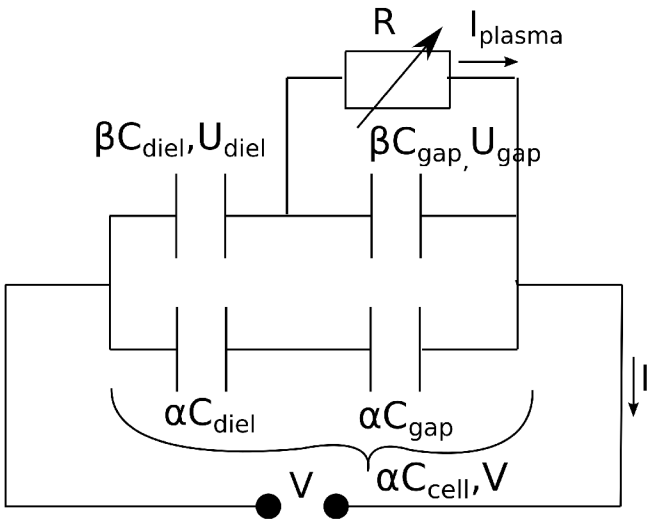


Figure 1.11: Alternative equivalent circuit. Reconstructed from[17].

equivalent circuit. It can therefore be described by following equations:

$$Q(t) \pm \frac{Q_0}{2} = \beta C_{cell} V(t) \text{ for sides AB, CD,} \tag{1.18}$$

$$Q(t) = \beta C_{diel}(V(t) \pm U_{gap}) \text{ for sides BC, DA.} \tag{1.19}$$

In case (b), slope of EF and GH is $C_{cell}$. For sides FG and HE, new capacitance $\zeta_{diel}$, which accounts for both non-discharging branch and dielectric capacitance of discharging branch, must be defined.

$$\zeta_{diel} = \alpha C_{cell} + \beta C_{diel} \tag{1.20}$$

Equations for parallelogram (b) will take form of:

$$Q(t) \pm \frac{Q_{00}}{2} = C_{cell} V(t) \text{ for sides EF, GH,} \tag{1.21}$$

$$Q(t) = \zeta_{diel}(V(t) \pm U_{gap}) \text{ for sides FG, HE.} \tag{1.22}$$

$Q_{00}$ is a charge variation on a DB for case (b). Analogically to previous circuit, relation between $Q_0$ and $Q_{max}$ (charge transferred during discharge in parallelogram (b)) can be obtained:

$$Q_0 = \left(1 - \frac{C_{cell}}{\zeta_{diel}}\right) Q_{max}. \tag{1.23}$$

$Q_{max}$ does not equal $q_{max}$. Their difference is $\alpha C_{cell} \Delta V$, where $\Delta V$ is voltage variation during discharge.

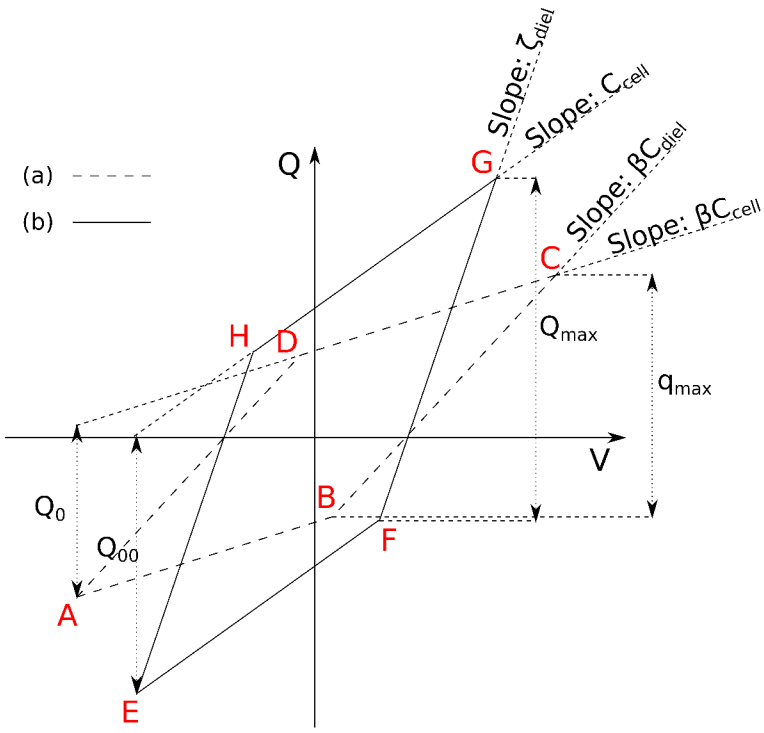


Figure 1.12: Q-V plots for alternative equivalent circuit.(a) With $\beta = 1$, (b) with arbitrary $\beta$. Reconstructed from[17].

## 1.5 Calculations of plasma driven chemistry

Chemistry in our experiment shall be described by calculation of transport coefficients and rate coefficients of chemical reactions present around the triple junction. These are the coefficients present in collision terms in basic equations of the fluid model of plasma, namely the continuity equation, Boltzmann equation and the transport equation. For this purpuse, online Boltzmann equation solver BOLSIG+ will be used. Developed by Gerjan Hagelaar in 2005, it is the replacement for older solver BOLSIG. It is aimed to remove flaws present in other solvers, such as applicability only to a narrow range of discharge conditions or limiting the accuracy of the fluid model with their approximations [18]. Transport and rate coefficients of electrons depend mainly on electron energy distribution function. This function can be calculated from collision cross sections by solving Boltzmann equation:

$$\frac{\partial f}{\partial t} + \vec{v}\nabla f - \vec{E}\frac{e}{m}\nabla_{\vec{v}} f = C[f], \tag{1.24}$$

where $f$ is the electron distribution function in position-velocity space, $\nabla_{\vec{v}}$ is the velocity gradient and $C[f]$ represent the rate of change of $f$ due to collisions. For simple conditions like in our case,rate and transport coeffcients can be tabulated as a functions of reduced electric field $E/N$, where $N$ is given particle density. This table is obtained by solving Boltzmann equation (BE) for several values of $E/N$. Values of the coefficient are then gathered by interpolating tabled data.

BOLSIG+ uses harsh approximations to solve BE. $f$ and $\vec{E}$ are considered uniform in the mean free collision path. $f$ is then symmetrical aroud direction of $\vec{E}$ in velocity space and varies only in this direction for position space. BE is then solved in spherical coordinates. Two term approximation for $f$ divides it into isotropic part $f_0$ and anisotropic part $f_1$ (a perturbation):

$$f(v, \cos\theta, z, t) = f_0(v, z, t) + f_1(v, z, t)\cos\theta. \tag{1.25}$$

$\theta$ is spherical coordinate representing angle between $\vec{E}$ and $\vec{v}$. Terms for $f_0$ and $f_1$ can be found from BE in spherical coordinates. By substitution, multiplication by Legendre polynomials and integration over $\cos\theta$ two equations are obtained, one of which contains overall momentum transfer cross-section consisting of contributions from all possible interactions $k$ with gas particles:

$$\sigma_m = \sum_k x_k \sigma_k, \tag{1.26}$$

where $x_k$ is the mole fraction of the target species, $\sigma_k$ is the effective momentum-transfer cross-section. Types of interactions considered by BOLSIG+:

- elastic collisions,
- excitation/deexcitation,
- ionization/attachment,
- electron-electron collisions.

For further simplification of $f_0$ and $f_1$ certain assumptions are made about their spatial and temporal dependence. They cannot be constant in both time and space, because processes like ionization do not conserve total numbers of electrons. Two cases for electron density growth are considered: *Exponential temporal growth without space dependence* which corresponds to pulsed townsend experiments and *Exponential spatial growth without time dependence* corresponds to steady-state townsend experiments.

Rate coefficients appearing in source terms of fluid equations can be most straitforwardly defined as:

$$k_k = \gamma \int_0^\infty \epsilon \sigma_k F_0 d\epsilon. \tag{1.27}$$

Here $\gamma = (\frac{2e}{m})^{1/2}$ is a constant ($m$ and $e$ are mass of an electron and elementary charge), $\epsilon = (\frac{v}{\gamma})^2$ is electron energy and $F_0$ is the energy distribution function. From there, reaction rate for collision procces $k$ is:

$$R_k = k_k x_k N n, \tag{1.28}$$

where $n$ and $N$ are electron and raecting species densities. Alternatively, Townsend coefficients $\alpha_k$ can be defined in units of inverse length such that:

$$R_k = \alpha_k x_k |\Gamma|, \tag{1.29}$$

where $\Gamma$ is the electron flux. These coefficients then take form:

$$\alpha_k = \frac{k_k \alpha N}{\tilde{v}_i}, \tag{1.30}$$

$$\alpha_k = \frac{k_k N}{\mu E}, \tag{1.31}$$

for the cases of only temporal and only spatial growth mentioned above (respectively). $\tilde{v}_i$ here is net production frequency of electrons and $\mu$ is their mobility. *It is recommended to use rate coefficients in situations where the electrons diffuse against the electric force (plasma bulk) and Townsend coefficients in situations where the flux is field driven* [18]. It is necessary to mention that BOLSIG+ only calculates initial electron driven reactions, not reactions of new produced species. Detailed information about BOLSIG+ calculations can be found in [18].

# 2 Experimental setup

Two different setups were examined, because, as will be discussed later on, the first setup brought inconclusive results. Despite this fact, it is still worth a discussion.

The configuration of a discharge cell in the first setup is sketched on figure 2.1 on the left. A fused silica tube, which served as a dielectric barrier was partially submerged in deionized water. Inner electrode was placed above water level, while outer electrode was completely submerged. Inner side of the tube was filled with transformer oil in order to prevent discharges on the inner side. Discharges took place in air near the surface of the outer side of the tube, that is, from the water surface to the area around the tip of inner electrode.

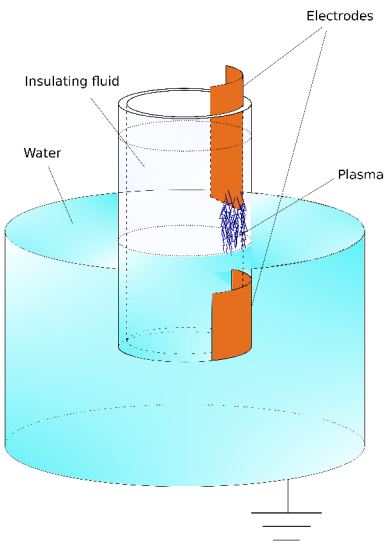


Figure 2.1: Sketched setup for experiment with deionized water.

The second examined setup, photographed on figure 2.2 is horizontaly symmetric around the center. Two planar electrodes (one with significantly larger covering area) are separated by a 1,2 mm thick $Al_2O_3$ with 92 % purity, which serves as a DB. Metal bar at the center serves as a contact for electrodes. Discharges appeared on the top side of the setup forming a radially symmetrical discharge area from the top electrode to some point not exceeding the edge of the bottom electrode. Experiment was conducted in ambient

air. This experiment was conducted by Mgr. Petr Synek, Ph.D., kindly provided the examined data.

For measurement of current and voltage for mean reduced electrical field determination, the following pieces of apparatus were used for both setups. Waveform generator *Agilent 33220A 20MHz* was used to generate a sine voltage function. For the voltage measurement *Tektronix P6015A* voltage probe with bandwidth of 75MHz was used. For the measurement of current, a current probe *Tektronix CT2* was used. This probe is Rogowski coil based with a bandwidth of 1,2 kHz–200MHz, sensitivity of 1 mV/1 mA with a $\pm$ 3% accuracy. Probes were connected onto oscilloscope *Keysight DSO-S 204A Digital Storage oscilloscope 20GSa/s, 10bit ADC*. Waveform generator was powered by *Lifetech* power source with a 0–30 kV range.

For spectrometric measurement, provided by Mgr. Lukáš Kusýn, setup similar to that on fig. 1.7 was used. Measurement was conducted by the CCS method mentioned in section 1.3. This method provided us with temporal profile of the discharge intensity with very high resolution. Spectrometer used was *SpectraPro -500* from *Acton Research Corporation*. For signal filtration, optical grid 1200 #/mm with 300 nm blaze was used. The same oscilloscope as for current/voltage measurement was used and single photon counter used was *TCSPC Becker&Hickl SPC-150*, with photomultiplier *PMT PMC-100-4*.

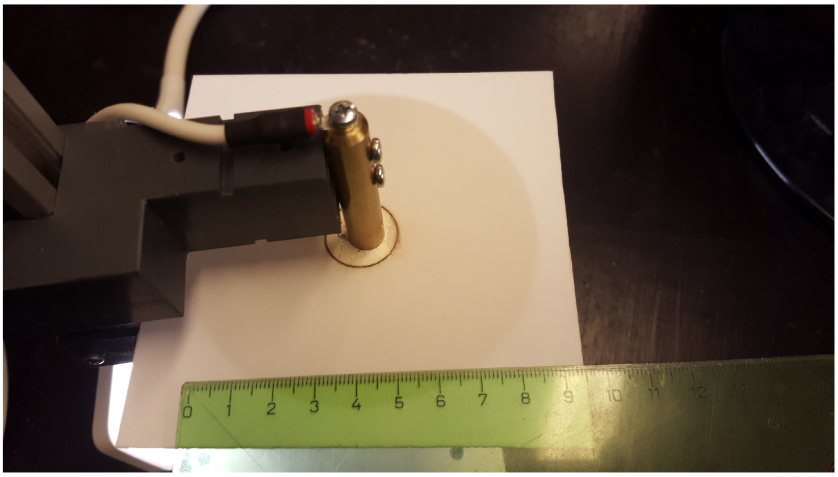

Figure 2.2: Setup for experiment with humid air.

# 3 Theoretical clarifications of measured quantities

## 3.1 Simplest equivalent circuit

**Macroscopic approach.** For simplest equivalent circuit, relations describing important quantities, namely gap voltage $U_g$, discharge current $I_R$ and charge transferred by discharge $q$ will be derived. Derived equations schould preferably contain only measurable quantities, namely $V(t), I(t), Q(t), C_{cell}, C_d$. From figure 1.9 using Kirchhoff's laws, following equations can be obtained:

$$U_d(t) = \frac{Q(t)}{C_d}, \tag{3.1}$$

$$U_g(t) = \frac{Q_g(t)}{C_g} \rightarrow \frac{\mathrm{d}U_g(t)}{\mathrm{d}t} = \frac{I_g(t)}{C_g}, \tag{3.2}$$

$$U_g(t) = V(t) - U_d(t), \tag{3.3}$$

$$I_g(t) = I(t) - I_R(t). \tag{3.4}$$

Substituing from equation (3.1) into equation (3.3) we get:

$$U_g(t) = V(t) - \frac{Q(t)}{C_d}. \tag{3.5}$$

By further substituing from equation (3.5) into equation (3.2) $I_g$ is obtained:

$$I_g(t) = C_g \cdot \left( \frac{\mathrm{d}V(t)}{\mathrm{d}t} - \frac{I(t)}{C_d} \right). \tag{3.6}$$

Finally, substituing equation (3.6) into equation (3.4) provides us with relation for $I_R$:

$$I_R(t) = I(t)(1 + \frac{C_g}{C_d}) - C_g \frac{\mathrm{d}V(t)}{\mathrm{d}t} = \frac{1}{1 - \frac{C_{cell}}{C_d}} \left( I(t) - C_{cell} \frac{\mathrm{d}V(t)}{\mathrm{d}t} \right). \tag{3.7}$$

Here, equation (1.7) was used for rewriting the prefactor. Charge transferred by discharging $q$ can be obtained by integrating relation (3.7):

$$q(t) = \frac{1}{1 - \frac{C_{cell}}{C_d}} \left( Q(t) - C_{cell} V(t) \right) + q_0. \tag{3.8}$$

**Microscopic approach.** Another approach on how to obtain these equations is via microscopic point of view. For simplicity, plain parallel electrodes will be considered. Current density in an arbitrary point on the electrode surface $j$ is a sum of conduction current density $j_c$ and displacement current density $j_d$. With considering linear constitutive relations it can be written as:

$$j(t) = j_c(x,t) + j_d(x,t) = j_c + \epsilon_0 \epsilon_r(x) \frac{\partial E(x,t)}{\partial t}. \tag{3.9}$$

Because capacitor plates are parallel, this relation can be rewritten in terms of macroscopic currents:

$$\frac{I(t)}{A} = \frac{I_c(x,t)}{A} + \epsilon_0 \epsilon_r(x) \frac{\partial E(x,t)}{\partial t}, \tag{3.10}$$

where $A$ is the electrode surface area. We now divide equation (3.10) by $\epsilon_0 \epsilon_r(x)$ and then perform integration through discharge cell, with x axis being perpendicular to electrode surfaces.

$$\begin{aligned}
&\int_0^{g+d} \frac{I(t)}{A\epsilon_0\epsilon_r(x)} \mathrm{d}x = \int_0^{g+d} \frac{I_c(x,t)}{A\epsilon_0\epsilon_r(x)} \mathrm{d}x + \frac{\partial}{\partial t} \int_0^{g+d} E(x,t) \mathrm{d}x \\
&\frac{I(x,t)}{A\epsilon_0} \left( \int_0^{g} \frac{1}{\epsilon_r(x)} \mathrm{d}x + \int_g^{g+d} \frac{1}{\epsilon_r(x)} \mathrm{d}x \right) = \frac{1}{A\epsilon_0} \left( \int_0^{g} \frac{I_c(x,t)}{\epsilon_r(x)} \mathrm{d}x + \right. \\
&\qquad\qquad \left. + \int_g^{g+d} \frac{I_c(x,t)}{\epsilon_r(x)} \mathrm{d}x \right) + \frac{\mathrm{d}V(t)}{\mathrm{d}t} \\
&\frac{I(t)g}{A\epsilon_0} + \frac{I(t)d}{A\epsilon_r} = \frac{I_c(t)g}{A\epsilon_0} + \frac{\mathrm{d}V(t)}{\mathrm{d}t}
\end{aligned}$$

Here $g$ is width of a gas gap and $d$ width of a DB. Inside interval [0,g], $\epsilon_r(x) = 1$ and inside interval [g,g+d] $\epsilon_r(x)$ is equal to $\epsilon_r$. Current $I_c(x,t)$ is constant on the interval [0,g] i.e. $I_c(x,t) = I_c(t)$ and on the interval [g,g+d] $I_c(x,t) = 0$, because no conductive current flows through the DB. Capacitance of a parallel plate capacitor is given by $C = A\epsilon_0\epsilon_r/l$, where $A$ is area of the plates and $l$ is the distance between them. Using this relation we can further write:

$$\frac{I(t)}{C_g} + \frac{I(t)}{C_d} = \frac{I_c(t)}{C_g} + \frac{\mathrm{d}V(t)}{\mathrm{d}t} \tag{3.11}$$

From the equation (3.11) using relation (1.7) we obtain:

$$I_c(t) = \frac{C_g}{C_{cell}} \left( I(t) - C_{cell} \frac{\mathrm{d}V(t)}{\mathrm{d}t} \right) = \frac{1}{1 - \frac{C_{cell}}{C_d}} \left( I(t) - C_{cell} \frac{\mathrm{d}V(t)}{\mathrm{d}t} \right),$$

which is the same as relation for $I_R$ (3.7). By integration we would get equation (3.9).

**Improvement of the method.** Up to this point, equations has been derived for VBDs. If they are to be used for SBD, a certain adjustment has to be made. In SBD, $C_g$ will decrease with rising distance from upper electrode. As was mentioned in section 1.2.2, charge accumulation in certain point on DB surface will eventually reach saturation level and charge deposition will be possible only at larger distances from the cathode; uniform charge layer will be created. Differences in $C_g$ are therefore caused only by electric field induced by electrodes. Flux lines are depicted on figure 3.1. There is also displacement current flow between electrodes, where no gas gap is present, thus it is not accounted for in simplest equivalent circuit scheme (fig. 1.9). These parasitic effects can be taken care of by adding a parallel capacitance $C_e$ into the circuit (see fig. 3.2). This approach is proposed by Pai et al. in [19].

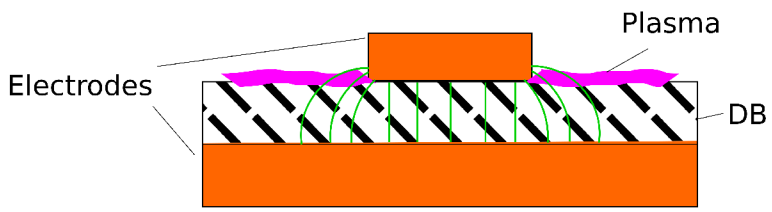


Figure 3.1: Symmetric SBD arrangement. Flux lines of electric field induced by capacitance $C_e$ represented by green lines.

By adding $C_e$ into the circuit, equations (3.1) and (3.4) will become:

$$U_d(t) = \frac{Q(t) - Q_e(t)}{C_d}, \tag{3.12}$$

$$I_g(t) = I(t) - I_R(t) - I_e(t). \tag{3.13}$$

Then, by the same process as before, equivalent relations with (3.5), (3.7) and (3.9) can be derived:

$$U_g(t) = V(t) - \frac{Q(t)}{C_d} + \frac{Q_e(t)}{C_d}, \tag{3.14}$$

$$I_R(t) = \frac{1}{1 - \frac{C_{cell}}{C_d}} \left( I(t) - I_e - C_{cell} \frac{\mathrm{d}V(t)}{\mathrm{d}t} \right) = \frac{1}{1 - \frac{C_{cell}}{C_d}} \cdot$$

$$\cdot \left( I(t) - (C_e + C_{cell}) \frac{\mathrm{d}V(t)}{\mathrm{d}t} \right), \tag{3.15}$$

$$q(t) = \frac{1}{1 - \frac{C_{cell}}{C_d}} \left( Q(t) - (C_e + C_{cell}) V(t) \right) + q_0. \tag{3.16}$$

It is good to define $C_e$ even for VBD between parallel plates, where it would account for the fact that electrodes are not infinitely large and non-homogenous field therefore exists beyond the electrode egdes. However, its value would definitely not be the same as in radially symmetrical SBD configuration. Circuit with $C_e$ will not be used in this thesis. Although providing better approximation, $C_e$ is hard to estimate. We will instead stick to the original simplest equivalent circuit and assess its validity for SBD.

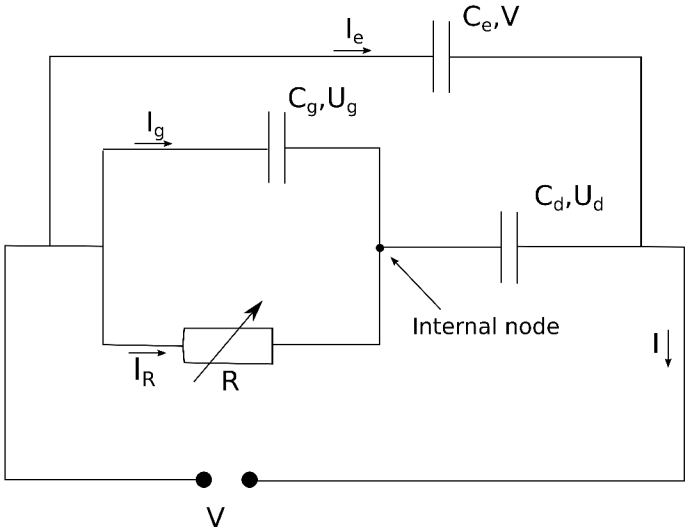


Figure 3.2: Simplest equivalent circuit with added electrode capacitance $C_e$.

## 3.2 Alternative equivalent circuit

Same derivation as in previous section will be done for alternative circuit. Electrode capacitance $C_e$ will be added right away. New scheme is shown on figure (3.3). Firstly, we consider equations (1.15)–(1.17), which remain the same. Secondly, using Kirchhoff's laws we obtain:

$$\frac{\mathrm{d}q_{diel}(t)}{\mathrm{d}t} = \frac{\mathrm{d}Q(t)}{\mathrm{d}t} - \frac{\mathrm{d}q_{cell}(t)}{\mathrm{d}t} - I_e(t), \tag{3.17}$$

$$I_{plasma}(t) = \frac{\mathrm{d}q_{diel}(t)}{\mathrm{d}t} - \frac{\mathrm{d}q_{gap}(t)}{\mathrm{d}t}, \tag{3.18}$$

$$U_{gap}(t) = V(t) - U_{diel}(t). \tag{3.19}$$

By substituing (3.17) into (3.18) and further substitutions for $q_{diel}$ and $q_{gap}$ from relations (1.16), (1.17), relation for discharge current $I_{plasma}$ is obtained:

$$I_{plasma}(t) = \left(1 + \frac{C_{gap}}{C_{diel}}\right)\left(\frac{\mathrm{d}Q(t)}{\mathrm{d}t} - \alpha C_{cell}\frac{\mathrm{d}V(t)}{\mathrm{d}t} - I_e(t)\right) - \beta C_{gap}\frac{\mathrm{d}V(t)}{\mathrm{d}t}. \tag{3.20}$$

By making use of equation (1.7) and the fact that $\alpha + \beta = 1$ and $\frac{\mathrm{d}Q(t)}{\mathrm{d}t} = I(t)$ final expression for $I_{plasma}$:

$$I_{plasma}(t) = \frac{1}{1 - \frac{C_{cell}}{C_{diel}}}\left(I(t) - (C_e + C_{cell})\frac{\mathrm{d}V(t)}{\mathrm{d}t}\right). \tag{3.21}$$

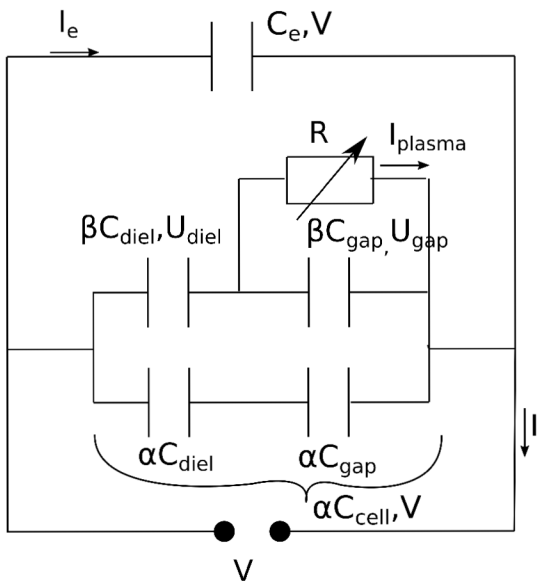


Figure 3.3: Alternative equivalent circuit with added electrode capacitance $C_e$.

Charge transferred by discharging $q$ can be again obtained by integration of discharge current (3.21):

$$q(t) = \frac{1}{1 - \frac{Ccell}{C_{diel}}}\left(Q(t) - (C_e + C_{cell})V(t)\right) + q_0. \tag{3.22}$$

For obtaining $U_{gap}$, let us substitute for $q_{diel}$ from (3.17) into (1.15) and then (1.15) into (3.19).

$$\begin{aligned} U_{gap}(t) &= V(t) - \frac{\int \frac{\mathrm{d}Q(t)}{\mathrm{d}t} - \frac{\mathrm{d}q_{cell}(t)}{\mathrm{d}t} - I_e(t)\mathrm{d}t}{\beta C_{diel}} = \\ &= V(t) - \frac{1}{\beta C_{diel}}(Q(t) - q_{cell} - q_e + q_1) \end{aligned} \tag{3.23}$$

Charges are obtained from measured currents by numerical integration. This integration is very sensitive to small systematic errors, which would lead to error accumulation with each discharge period. As stated in [16], this can be adressed by two approaches:

1. Charge at time zero is equal to zero.
2. Average charge transferred over natural number of full periods is equal to zero.

In [16], second approach was chosen and so it will be here. In a high numbers of voltage periods, integration constant $q_1$ will average to zero. By substituing for $q_{cell}$ from equation (1.15) and $q_e = VC_e$ following equation is obtained:

$$U_{gap}(t) = V(t)\left(1 + \frac{\alpha C_{cell} + C_e}{\beta C_{diel}}\right) - \frac{Q}{\beta C_{diel}} \tag{3.24}$$

Microscopic approach would again lead to same results if capacitance $C_e$ is treated as parallel plate capacitor. Alternative equivalent circuit would probably provide better results than simplest equivalent circuit. Unfortunately, determination of coefficients $\alpha$ and $\beta$ is not possible with current setup. In the setup with radially symmetrical electrodes, grounded electrode is much larger than the other one, thus the discharge does not extend to its edge. In SBDs, especially with covered cathode, discharge area is not precisely defined, it is therefore not possible to estimate $\alpha$ and $\beta$ coefficients. If we were to increase applied voltage to such extent that discharge area would cover whole electrode, spark discharge would be ignited and characteristics of the discharge would drastically change. In regard to tube setup, it would probably be possible to estimate $\alpha$ and $\beta$ if we would consider discharging area starting at the tip of inner electrode. However, as it will be seen in the next chapter, this experiment provided results for which it is not possible to calculate $C_d$, $C_{cell}$. We will therefore stick to the simplest equivalent circuit.

## 3.3 Capacitances

In section 1.4 it was mentioned that although it is assumed by classical theory, $U_g$ is not constant during the discharge. This is due to small size of our experiment, in which $U_g$ drops over individual microdischarges will be strongly pronounced. Also, in configuration on figure 2.2 the discharge area grows during the discharge, which changes both capacities $C_d$ and $C_g$. Figure 3.4 with a depicted typical Q-V plot observed for SBD configuration shows non-linear development during the discharge phase. However, due to the accumulation of the charge on the dielectric barrier and following exhaustion of the discharge activity, transferred charge is limited and maximum of $Q(t)$ depends only on $V(t)$ amplitude. Residual gap voltage $U_{res}$ at the point $[V_{max}, Q_{max}]$ schould therefore be independent of value $V_{max}$. Instead of determination of $C_d$ as a slope of side BC or DA of the parellelogram (fig. 1.10), it is to be determined as a slope of linear fit of points $[V_{max}, Q_{max}]$ for different values of $V_{max}$. When it comes to capacitance $C_{cell}$, it can be freely determined as a slope of AB or CD side of the Q-V plot, as during non-discharging phase $U_g = 0$.

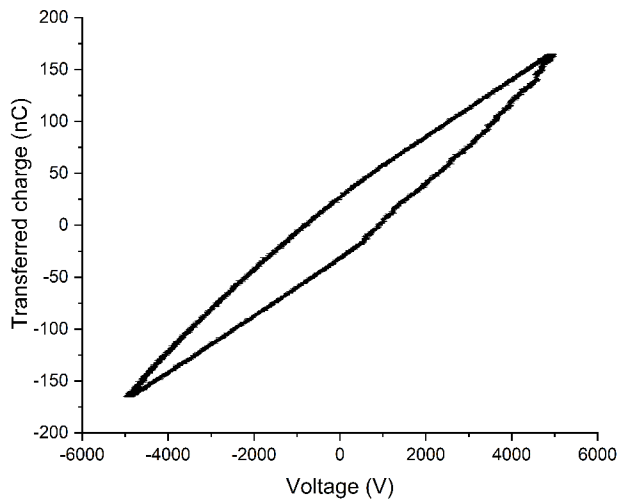


Figure 3.4: Example of Q-V plot for SBD. Measured in the experiment with humid air.

## 3.4 Electric field

If one were to consider uniform electric field in the gas gap, it would be simply calculated by:

$$E = \frac{U_g}{d}, \tag{3.25}$$

where $d$ is the electrode distance. However, during a streamer phase, most of the electric field disturbance happens in close vicinity of the edge of the streamer. Quasineutral streamer channel on the other hand experiences zero electric field and acts as a prolonged electrode. In [1] a 2D simulation of

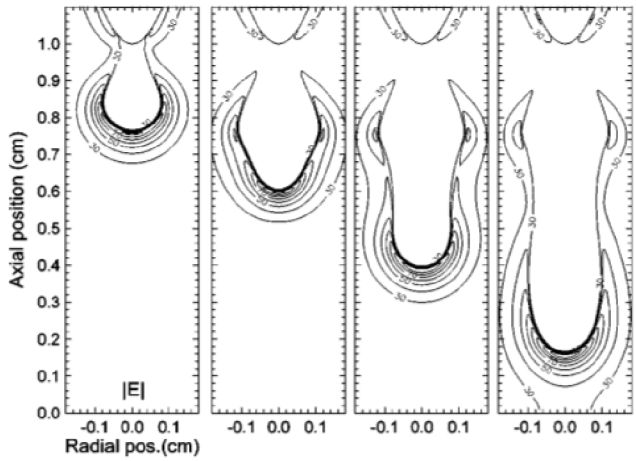


Figure 3.5: Result of simulation of absolute value of electric field taken from [1].

a propagating streamer based on calculating continuity equation has been made. Based on the results, streamer phase development was described as a small avalanche-to-streamer transition region ("streamer head") propagating towards cathode. Streamer head is considered to have approximately spherical shape, so is visible on figure 3.5. If parameter $x$ is introduced, such that $x = z_{max} - z$, where $z_{max}$ is he point of maximum $E$ and $z$ is the axial position on fig. 3.5, following distribution of $E$ can be considered:

$$E(x) = \begin{cases} E_{max}\left(1 + \frac{x}{R}\right), & -R \leq x \leq 0, \\ \dfrac{E_{max}}{1 + \frac{x}{2R}} & x \geq 0 \quad [1] \end{cases} \tag{3.26}$$

Here $R$ is the radius of the spherical head. As will be seen, this model provides peak profile very similar to measured 0-0 SPS of nitrogen profile and so it will be used to determine value of $E_{max}$.

# 4 Results and discussion

In this chapter experimental data processed with simplest equivalent circuit model will be shown and discussed. In section 4.1, experiment with configuration on figure 2.1 will be examined. It will be shown why it has brought inconclusive results and also possible reason will be stated.

Results of an experiment with radially symmetrical plain electrodes (2.2) will be shown in section 4.2. Different developments of current in positive and negative voltage half-periods will be discussed. Attention will be brought to positive half-period with stronger filamentary character. Note that bottom, wider electrode is grounded (in previous experiment it is the submerged electrode) and voltage $V$ is measured as a potential on top electrode. Basic electrical quantities will be calculated. Capacitances will be determined from a Q-V plot. Velocity of propagating streamer and effective radius of its head will be determined from provided spectroscopic measurement. Electrical field around the streamer head at the point in time when it is near the top electrode will be estimated from the $U_{gap}$ with model developed in [1]. Validity of the results will be discussed. Experimental setups are discussed in chapter 2.

In section 4.3, rate and transport coefficients will be calculated with the help of LXCat site and two cross-section databases will be compared.

## 4.1 Fused silica tube configuration

Results for the first setup with silica tube halfway submerged in water will now be discussed. Applied voltage $V(t)$ and current $I(t)$ were measured with sampling frequency 1 GS/s and voltage frequency $f = 13700$ Hz. One discharge cycle (current/voltage) period was chosen and examined. It was measured from the current function intercept with time axis before positive half-period. In section 3.2 in chapter 3 it has already been stated that we consider charge transferred over one full period equal to zero. Measured current was therefore adjusted so that $Q(t)$ graph starts and ends with the same value after one period. Measured voltage and current functions are shown on figure 4.1. Example of zoomed discharge current pulse is shown on figure 4.2. Oscillating behaviour is attributed to slight conductive property of water.

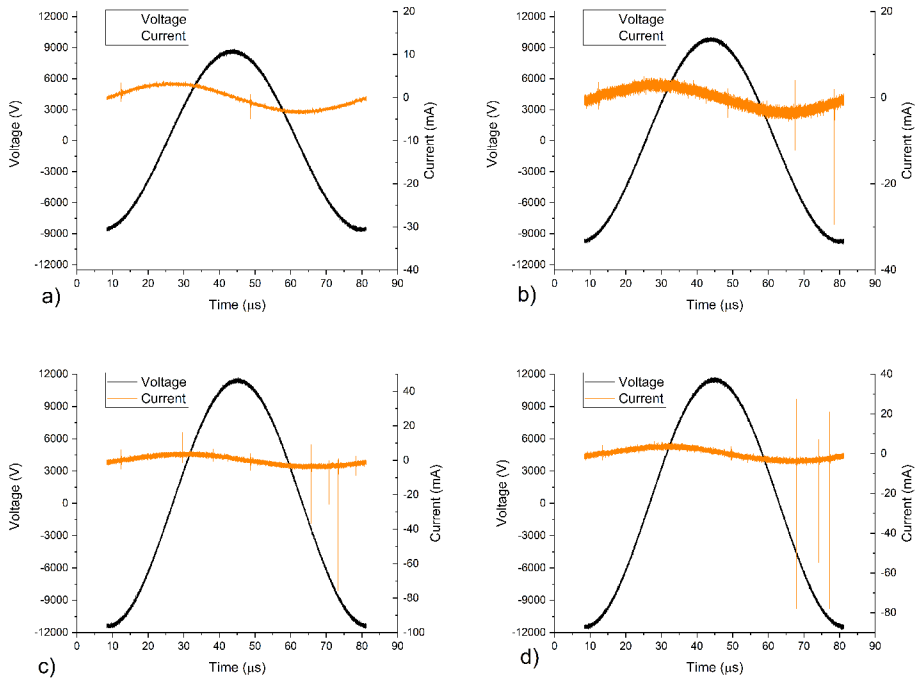


Figure 4.1: Graphs of measured current and voltage period in setup with water for various voltage amplitudes: a) 9 kV, b) 10 kV, c) 11 kV,d) 11,5 kV.

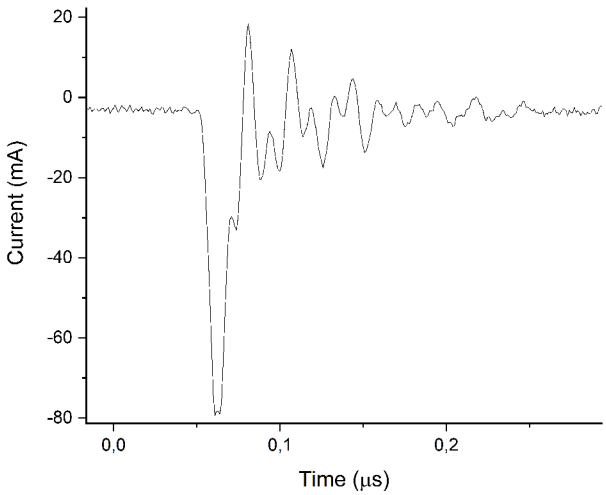


Figure 4.2: Example of peak profile in experiment with water.

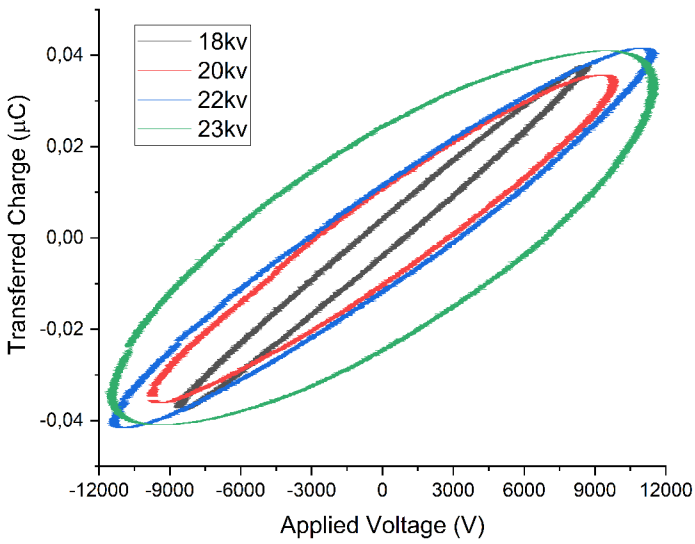


Figure 4.3: Lissajous figures for different peak to peak voltages obtained from experiment with water present.

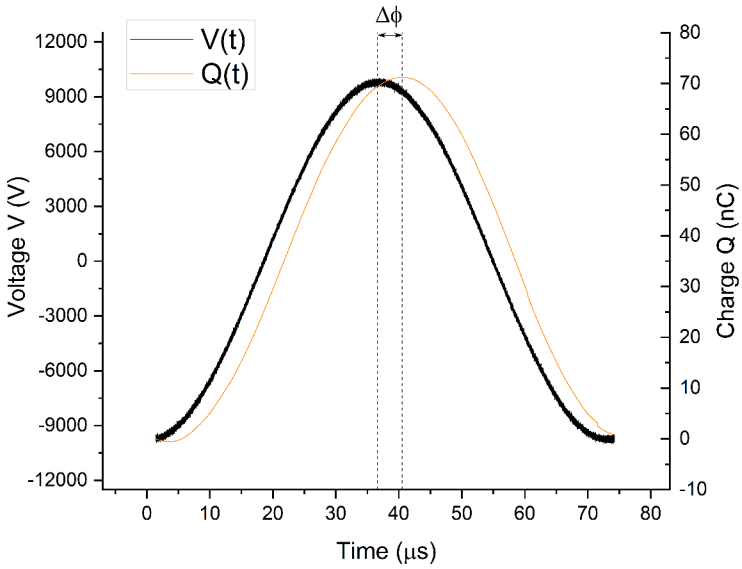


Figure 4.4: Measured charge and voltage over one period for $V_{max} = 10$ kV. Phase difference $\Delta\phi$ depicted by dashed lines.

Transferred charge $Q(t)$ was obtained by numerical integration of $I(t)$. Obtained Q-V plots are shown on figure 4.3. It is clear that their oval profile is not resembling typical Q-V plot (3.4). Non-discharge phase parts (right after charge extremes) schould be linear with a slope of $C_{cell}$. Points od charge maxima/minima for different applied voltages schould lay on one line, slope of which is $C_d$. None of the previous is true for measured data. It is therefore not possible to estimate capacities $C_{cell}$, $C_d$ needed for estimation of $E/N$. Reason for such profile of the Q-V plot lies in non-zero phase difference between $Q(t)$ and $V(t)$ (fig. 4.4). In [20], it was stated that energy efficiency fo a DBD reactor depends on phase difference of $Q(t)$, $V(t)$. Because energy transferred during a discharge cycle is given by area of a Q-V plot, it must get wider with rising efficiency; forming an oval shape. Out of this issue, a need for different setup–without the effect causing this issue–has arose. This effect is attributed to the fact that water is a little conductive. Electrons can ionize water molecules of its surface, which are then able to travel to the submerged electrode, changing the $C_d$ capacitance. The reason why $Q(t)$ and $V(t)$ should be in phase is that because of the capacitive character of the cell, current is ahead of voltage by $\pi/2$, but as current is a sine function, by integrating it this phase difference vanishes.

## 4.2 Radially symmetrical setup in humid air

This experiment was conducted for the need of changing properties described above, which are thought to be the cause of failure of previous experiment. Shape of electrodes was changed and water element replaced with humid air. Discharge was operating at the same frequency and with the same sampling frequency as in previous experiment. Same procedure was used. Typical current spike during discharge in positive voltage half-period is shown on figure 4.5. In contrast to previous experiment, no oscillations are to be seen.

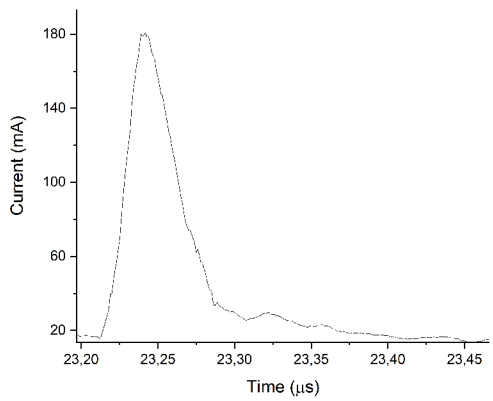


Figure 4.5: Typical peak profile in experiment with humid air.

Measured voltages and currents are shown on figure 4.6. It may seem that most of the discharge activity happens within positive voltage half-period. Such case would be a contradiction to premise considered in this work, that charge transferred over one full period is zero (see section 3.2). In figure 4.6, measured currents are overlapped with a sine function. This function has the same frequency and amplitude as applied sinusoidal current. Everything extending the sine function must be a result of a discharge activity. As it is clearly visible, discharge does occur in negative voltage period. However, it is rather continuous, whereas discharge occuring in positive voltage half-period has stronger filamentary character, resulting in discrete peaks in the graph. For higher applied voltages (figure 4.6d),e) ), discharge activity extends even over voltage minimum. This behaviour is caused by asymmetry in conducted experiment, as was discussed in section 1.2.2. Ex-

cept current spikes, which are relatively small compared to those in positive half-period, continuous current is observed. This is also in agreement with rise of minimal current with each microdischarge as the results have shown in [12]. For higher voltage amplitudes, this continuous current grew so rapidly that there was not enough time for it to be decreased back to zero until voltage minimum was reached. Discharging therefore continued a little after voltage minimum.

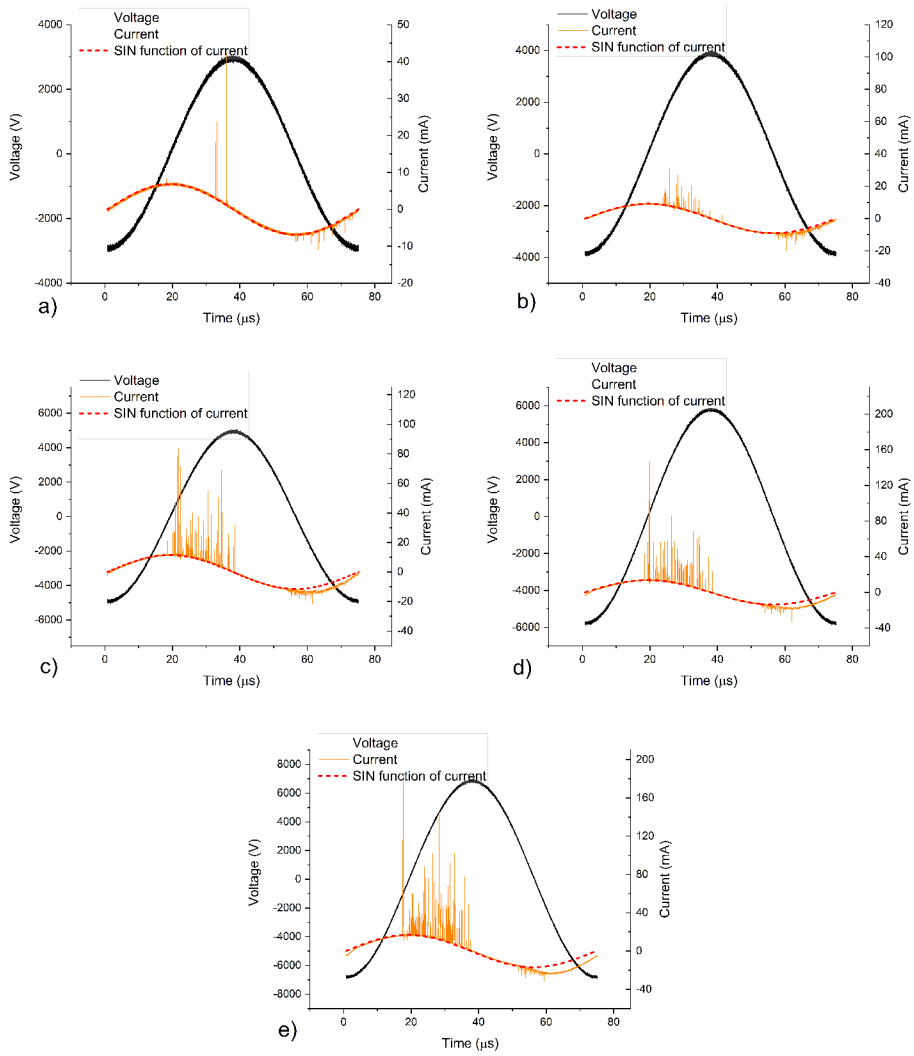


Figure 4.6: Graphs of measured current and applied voltage period in setup with humid air for various voltage amplitudes: a) 3 kV, b) 4 kV, c) 5 kV,d) 6 kV, d) 7 kV.

Q-V plots obtained provide much better result (fig. 4.7). Parts of the graphs right after points $Q_{max}$–$V_{max}$ and $Q_{min}$–$V_{min}$ are linear, which corresponds to a non-discharge phase. Also, points $Q_{max}$–$V_{max}$ can be fitted with a line. Therefore, capacitances $C_d$ and $C_{cell}$ could be derived (see section 3.3). Fitted lines are depicted on figure 4.7. $C_{cell}$ was determined for every value

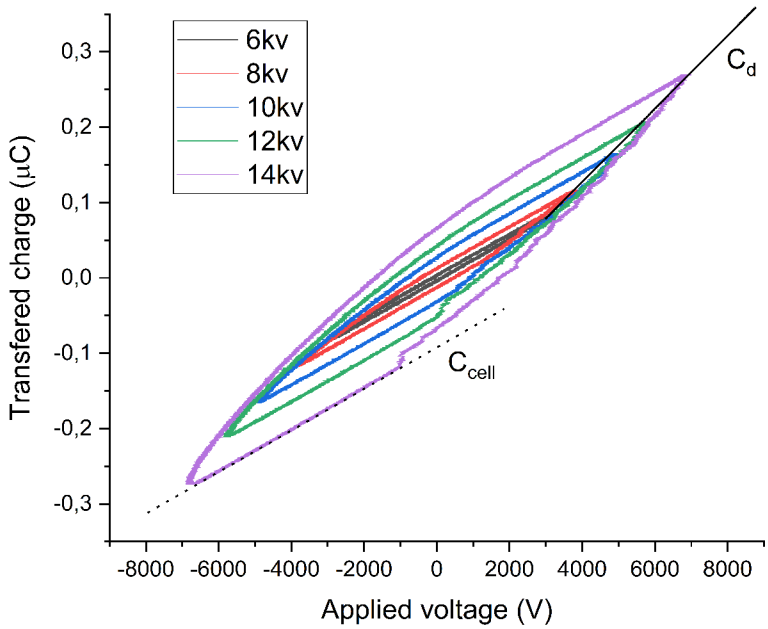


Figure 4.7: Lissajous figures obtained from planar experiment with humid air for different peak to peak voltages.

of $V(t)$ amplitude and averaged. $C_g$ was determined from the relation (1.7). Obtained capacitances are listed in table 4.1. Obtained Q-V plots are not symmetrical around point [0,0], namely, discharge phases have slightly different profiles for negative and positive half-period. This can again be explained by the asymmetry of the setup causing different character of the discharge depending on polarity of $V(t)$ (section 1.2.2). Plots do not take form of parallelograms, because of stair-like profile of positive half-period discharge phase. As discussed in section 1.4, $U_g$ is not constant during a discharge, but instead decreases with each microdischarge and increases with rising $V(t)$. Only in case when these two dependencies compensate will $U_g$ remain constant.

$U_g$ functions were obtained from equation 3.5 by subtituing measured $C_d$. Their graphs for each value of amplitude of $V(t)$ are shown on figure 4.8. Without discharge, $U_g$ would take form of a perfect sinusoid. Discharges however influence $U_g$ and so it will have a behaviour seen on the figure. To

obtain a single value of $E$, only a single value of $U_g$ is needed. The value chosen is the one at the point when discharge phase begins (just before first voltage drop). Because discharging activity starts in the region of triple junction, it is logical that most relevant value of $U_g$ will be at the discharge beginning. These points are indicated in fig. 4.8 by dotted lines. Values can be found in table 4.1. Different values arise from different amplitudes of $V(t)$ because of slight dependance of residual voltage in the gap $U_{res}$ ($U_g$ at the point $Q_{max}$–$V_{max}$) on $V(t)$ amplitude. Uncertainty of $U_g$ therefore depends on uncertainty of $C_d$ [16]. Equation (1.6) at point $Q_{max}$–$V_{max}$ takes form of:

$$Q_{max} = C_d(V_{max} - U_{res})$$

Parts of the uncertainties of $C_d$ and $U_{res}$ are uncertainties of parameters of linear fit. Note that no other types of uncertainties were accounted for. From the uncertainty of $U_{res}$ (tab. 4.1) it can be assumed that differences in $U_g$ for different $V$ amplitudes schould be in order of hundreds of volts, which is in agreement with our results. This kind of uncertainty for $C_{cell}$ happened to be insignificant, so it is not stated in table 4.1. Voltage drops for $V_{max} = 3$ kV were so small the beginning of the discharge could not be determined from the graph.

Table 4.1: Measured capacitances and gap voltages. Uncertainties in $C_d$, $U_{res}$ come solely from parameters of fitted line.

| $V_{max}$ (kV) | $C_{cell}$ (pF) | $U_g$ (V) | $C_d$ (pF) |
|---|---|---|---|
| 3 | 26,6 | – | $48 \pm 2$ |
| 4 | 27,1 | 1083 | $C_g$ (pF) |
| 5 | 27,0 | 870 | 61,5 |
| 6 | 27,0 | 1092 | $U_{res}$ (V) |
| 7 | 27,2 | 1453 | $1400 \pm 200$ |

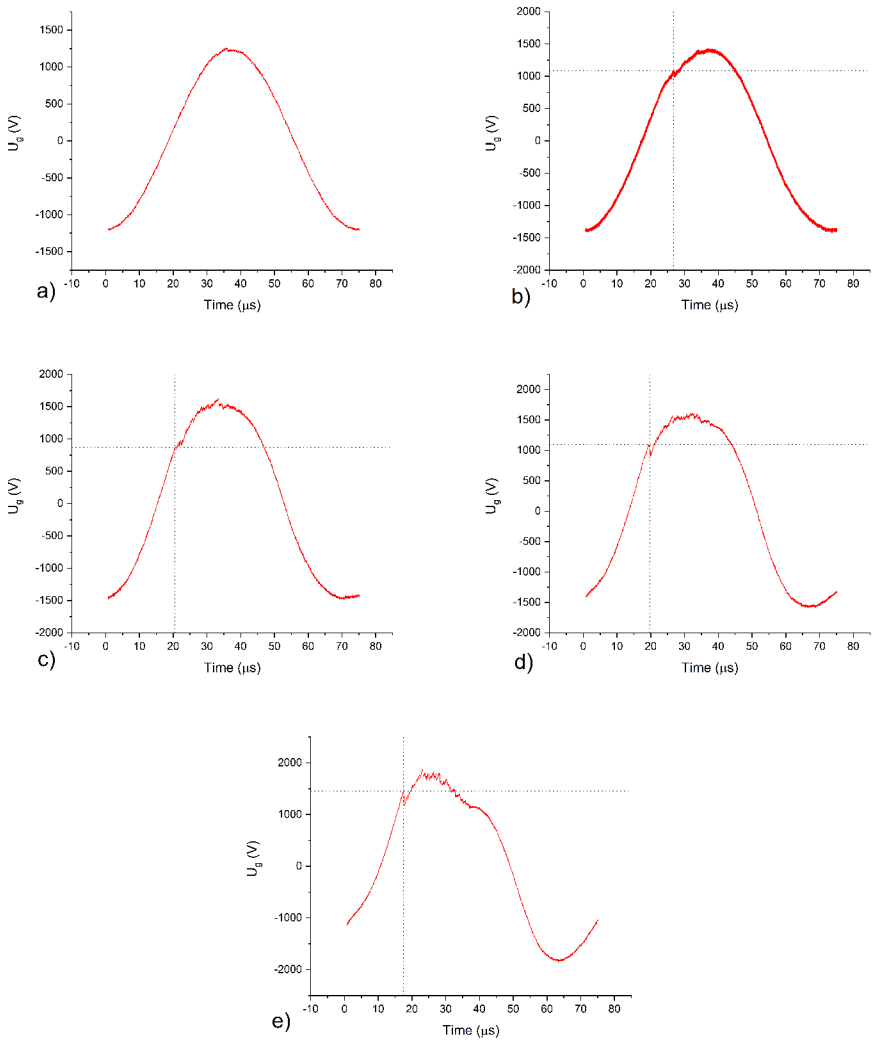


Figure 4.8: Gas gap voltages $U_g$ for various applied voltages $V$ (peak to peak): a) 6 kV, b) 8 kV, c) 10 kV,d) 12 kV, d) 14 kV.

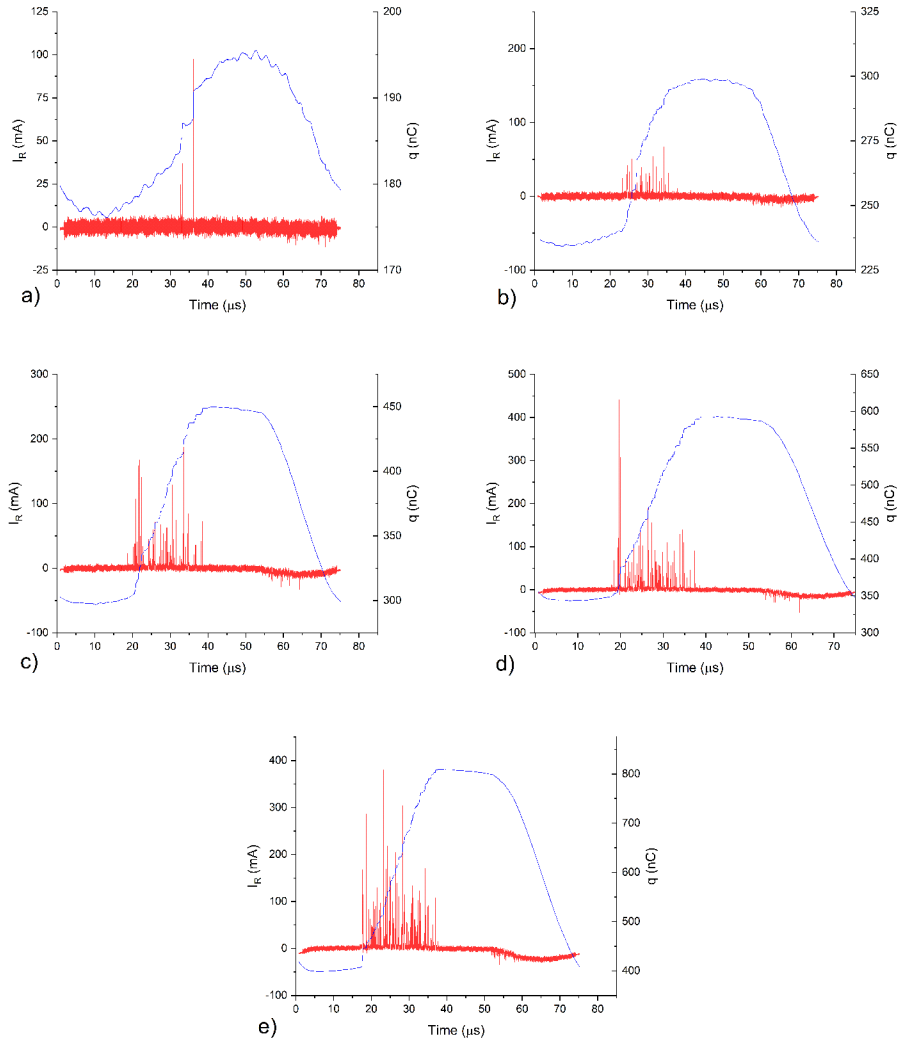


Figure 4.9: Current $I_R$ flowing through and net charge $q$ transferred through the discharge cell for different $V$ (peak to peak). a) 6 kV, b) 8 kV, c) 10 kV, d) 12 kV, e) 14 kV.

Discharge currents and charges transferred through discharging, calculated from equations (3.7) and (3.8) are shown on figure 4.9. As one would expect, $I_R$ does not have sinusoidal component caused by the displacement current; it is non-zero only during discharging. Its peak values are approximately 2 times higher than those of $I$. This can mathematically be explained by examining measured capacitances. Ratio $\frac{C_{cell}}{C_d} \approx \frac{1}{2}$ and so the prefactor in equation (3.7) is roughly 2. $I$ is therefore multiplied by 2, while the term with $C_{cell}\frac{\mathrm{d}V}{\mathrm{d}t}$ corresponds to sinusoid part of $I$ (fig. 4.6) with relatively small amplitude.

When it comes to $q$, it changes during the discharge activity and remains approximately constant during non-discharging phases. In figure 4.9a), discharge activity is so low that $q$ is strongly influenced by random noise. An interesting fact, is that although $I$ was adjusted so that its integral over one full period is zero (logically $I_R$ integral is too), $q$ is not symmetrical around zero. This fact is attributed to the non-zero integration constant in (3.8). To verify this claim, mean value of $q$ was calculated from maximum and minimum values of $q$ read from graphs. This is the value which needs to be subtracted to make $q$ symmetrical around 0. For the time coordinate of this mean value, $V(t)$ and $Q(t)$ values were obtained from measured data and integration constant calculated from equation (3.8). $q_0$ values are in agreement with mean $q$ value, which proves the supposed reason for the offset. These values are listed in table 4.2.

Table 4.2: Integration constants $q_0$ in equation (3.8).

| $V_{max}$ (kV) | $q_0$ (nC) |
|---|---|
| 3 | 185 |
| 4 | 362 |
| 5 | 369 |
| 6 | 469 |
| 7 | 603 |

To obtain effective value of $E$ we have to divide $U_g$ with effective streamer head length $R$. To obtain this quantity, optical measurement provided by Mgr. Lukáš Kusýn of SPS of nitrogen was analyzed. Relative intensity as a

function of time for two distances from the cathode is shown on figure 4.10. Note that these distances have no physical meaning, only their difference is important.

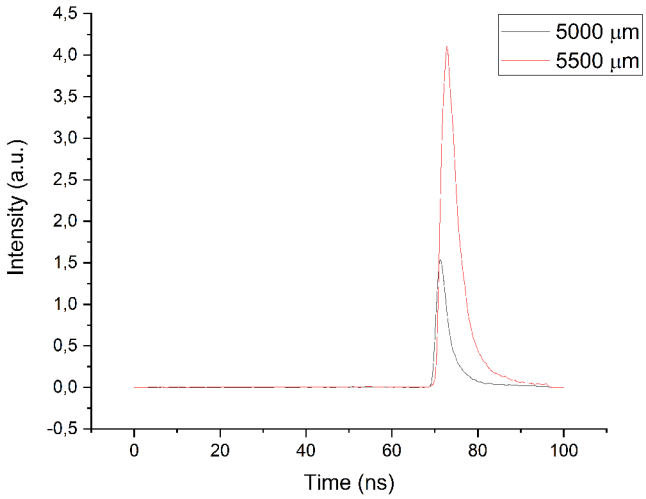


Figure 4.10: Measured intensity of 0-0 transition of SPS of molecular hydrogen (positive half-period). Measuring was conducted for 2 effective distances: 5 mm, 5,5 mm.

$R$ can be obtained from relation:

$$R = \frac{\tau}{v_s}, \tag{4.1}$$

where $\tau$ is duration length of a discharge and $v_s$ is velocity of a streamer. $\tau$ was determined as a difference between points at 90% and 10% of maximum value of intensity, because recombination is very low when streamer head arrives and reaches its maximum only after streamer head passes. Quantity $v_s$ was determined as a difference of distances from cathode divided by time difference of points with the same intensity value relative to the peak value. Values of $E$ determined this way are listed in first columns of table 4.3.

This way however, a step-like function $E(x)$ would be obtained. This is obviously not a very good approximation of electric field, as the profile of typical current peak looks like that on figure 4.10. So instead, to estimate $E$, relation (3.26) proposed by Kulikovsky in [1] was used. Functions were modeled with parameter $E_{max}$ being adjusted, so that integral over created

curve would give measured value of $U_g$. Chosen integration interval was from $-R$ to 5 mm. $E$ values obtained by simple division of $U_g$ by $R$ were used as an initial estimate for $E_{max}$. Results of this trial are again listed table 4.3. Final values of $E_{max}$ are one order of magnitude lower than initial values. Modeled $E$ function is shown on figure 4.11. For analyzing plasma driven

Table 4.3: Electric fields for the two distances in the gap. Initial field obtained from $E_{max} = U_g/R$. $E_{max}$ obtained from equation (3.26).

| Effective distance 5000 $\mu$m | | | | | $v_s$ (km/s) |
|---|---|---|---|---|---|
| $V_{max}$ (kV) | Initial $E_{max}$ (V/m) | Initial $E_{max}/N$ (Td) | $E_{max}$ (V/m) | $E_{max}/N$ (Td) | 250 |
| 4 | 3,12E+6 | 127,38 | 6,70E+5 | 27,38 | $R$ (5000 $\mu$m) |
| 5 | 2,50E+6 | 102,32 | 5,36E+5 | 21,90 | 347 |
| 6 | 3,14E+6 | 128,43 | 6,70E+5 | 27,38 | $R$ (5000 $\mu$m) |
| 7 | 4,18E+6 | 170,91 | 8,90E+5 | 36,39 | 451 |
| Effective distance 5500 $\mu$m | | | | | |
| $V_{max}$ (kV) | Initial $E_{max}$ (V/m) | Initial $E_{max}/N$ (Td) | $E_{max}$ (V/m) | $E_{max}/N$ (Td) | |
| 4 | 2,40E+6 | 98,11 | 5,68E+5 | 23,22 | |
| 5 | 1,93E+6 | 78,81 | 4,54E+5 | 18,56 | |
| 6 | 2,42E+6 | 98,92 | 5,68E+5 | 23,22 | |
| 7 | 3,22E+6 | 131,63 | 8,10E+5 | 33,11 | |

chemistry, reduced electrical field is needed. Gas in the gap was treated here as an ideal gas and volume concentration of neutral particles $N$ was calculated from ideal gas law $pV = NKT$. For atmospheric pressure and 300 K temperature it was obtained:

$$N = \frac{p}{kT} = 2,446314142 \cdot 10^{25}\ \mathrm{m}^{-3}$$

In [21] simulation of DBD was conducted. It was found that for positive streamer, peak values of $E$ reach 150-160 kV/cm. In [22], spectroscopic measurement using cross correlation spectroscopy was conducted on CBD. Observed peak value of $E/N$ was around 1200 Td. These values provide

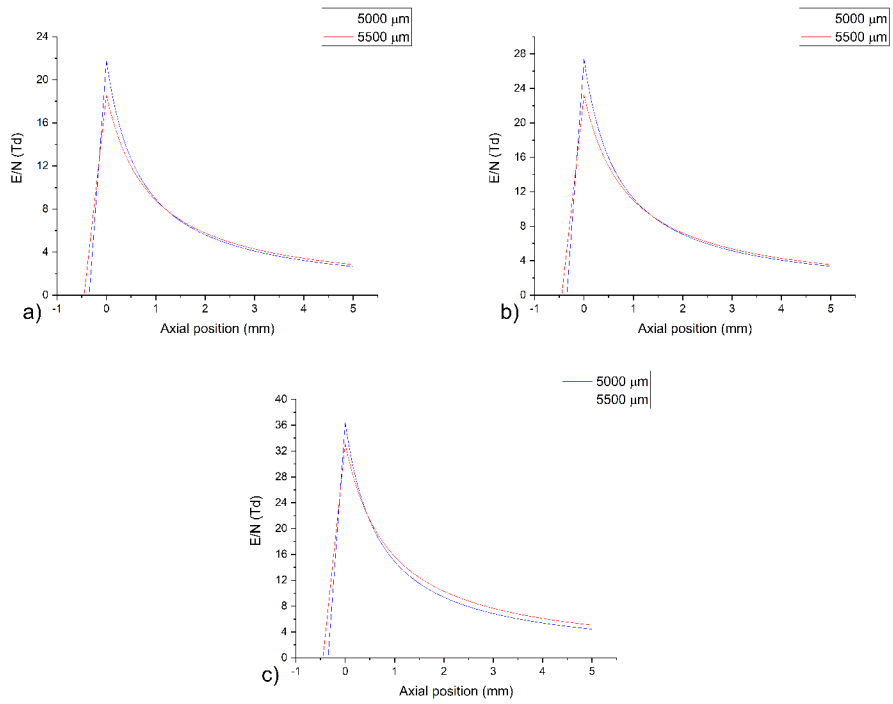


Figure 4.11: $E$ distribution modeled by (3.26). a) $U_g = 870$ V, b) $U_g = 1090$ V, c) $U_g = 1453$ V.

us with an idea of correct result. Unfortunately, values in table 4.3 are two orders of magnitude lower. Equivalent circuit model was therefore not sufficient, or additional uprades and considerations have to be made. Nevertheless, rate and transport coefficients could still be calculated with a value of $E/N$ closer to reality. The value 1200 Td from [22] was used.

## 4.3 Rate and transport coefficient analysis

For finding transport coefficients and rate coefficients of the ongoing reactions we turned to site `www.lxcat.net`. LXCat is an open-acccess online platform which uses BOLSIG+ described in section 1.5 for calculation of various types of data used for modeling low temperature, non-equilibrium plasmas. It uses various databases of cross-sections, so that user is able to obtain wanted data only by inserting gas temperature, reduced field $E/N$ and list of present species with respective mole fractions. Interval of minimum and maximum value of $E/N$ is divided into steps and coefficients are tabulated

in dependence on $E/N$.

As was mentioned in previous section, used maximum value of reduced electric field was $E/N = 1200\,\mathrm{Td}$. Altough measured for coplanar discharge, velocity of streamer head and mean field should not be much different, because discharge propagates along dielectric surface, just like SBD. As regards the list of species, ambient air of 20% oxygen and 80% nitrogen is considered with 100% for 300 K temperature. This is as close as we can get to triple junction involving water.

On figure 4.12, results for chosen transport coefficients are shown. Because our interest is in chemical reactions, ionization frequencies and coefficients were chosen along with mean electron energy. Results for rate coefficients are shown on figure 4.13. Chosen reactions are listed below. Most of them have either oxygen or hydroxyl radicals, or oxygen ions as a product. These species have very useful and broad range of applications. Hydroxyl atoms are widely used in radical chemistry and can be used for treatment of greenhouse gases such as CO or $CH_4$. Elemental oxygen is capable of generating ozone–an again very useful substance used in water treatment, cleaning of pullutants or decontamination of food packages. These applications are described in [23]. Chosen reactions:

1. ionization $e + H_2O \longrightarrow e + e + H_2O^+$,
2. attachment $e + H_2O \longrightarrow H^- + OH$,
3. attachment $e + O_2 \longrightarrow O^- + O$,
4. attachment $e + H_2O \longrightarrow H_2 + O^-$,
5. excitation $e + H_2O \longrightarrow e + H + OH$,
6. ionization $e + O_2 \longrightarrow e + e + O_2{}^+$.

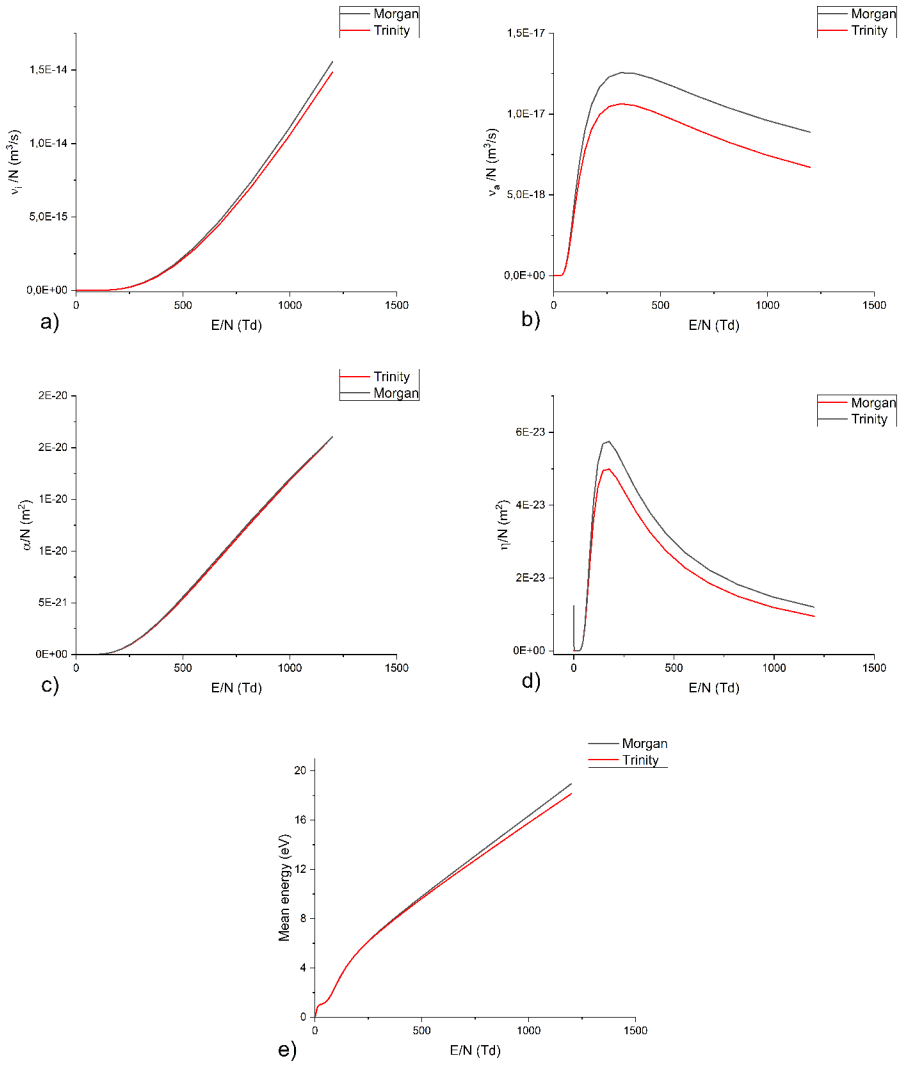


Figure 4.12: Calculated transport coefficients: a) total reduced ionization frequency, b) total reduced attachment frequency, c) Townsend ionization coefficient, d) Townsend attachment coefficient, e) Mean electron energy. Obtained from [24].

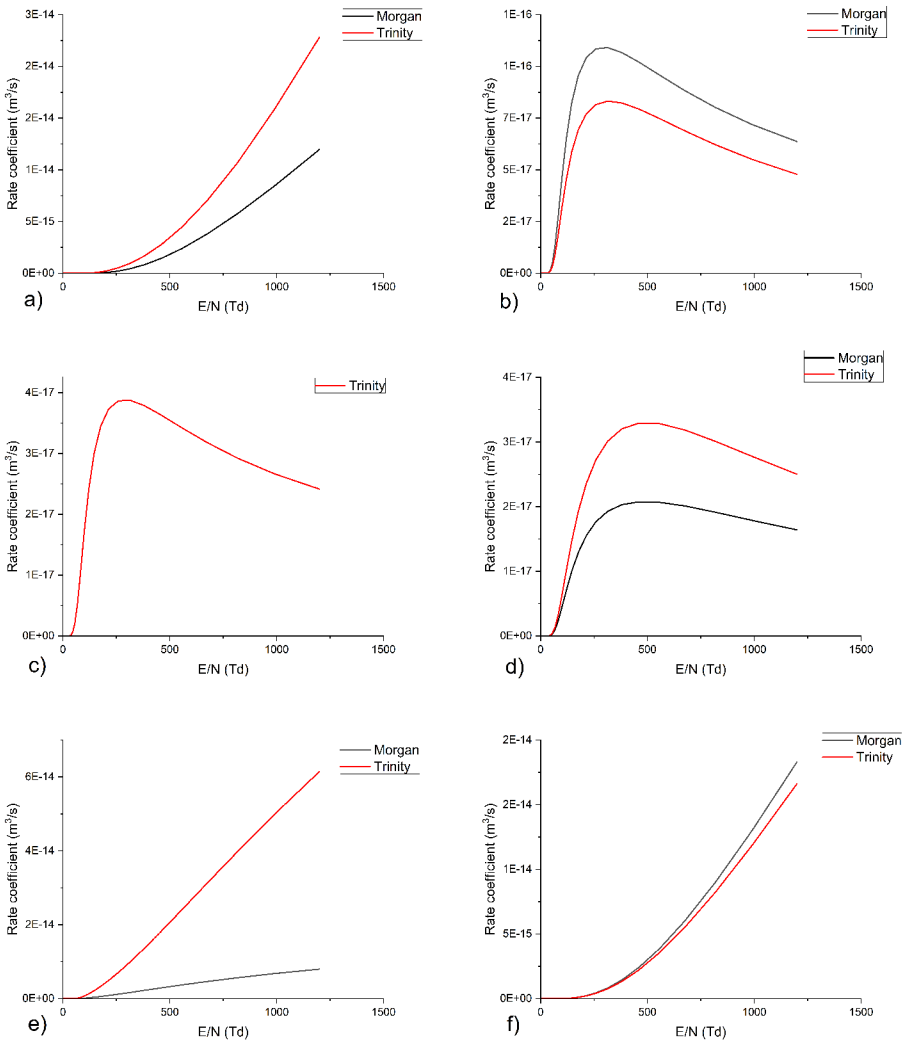


Figure 4.13: Calculated rate coefficients. Chosen reactions: a) ionization $e + H_2O \longrightarrow e + e + H_2O^+$, b) attachment $e + H_2O \longrightarrow H^- + OH$, c) attachment $e + O_2 \longrightarrow O^- + O$, d) attachment $e + H_2O \longrightarrow H_2 + O^-$, e) excitation $e + H_2O \longrightarrow e + H + OH$, f) ionization $e + O_2 \longrightarrow e + e + O_2{}^+$. Obtained from [24].

Calculation was conducted for two different cross-section databases: Morgan and TRINITY [25]. These are databases containing all species in our list, which consists of $N_2, O_2, H_2O$. The two databases are compared on figure 4.14. Morgan database is chosen as a reference and Trinity database is plotted as a set of multiplication factors, for which the measured data approximately coincide. For coefficients which do have a maximum, multiplication factor was chosen so that maxima of particular coefficient for different databases would coincide. Multiplication factors are listed in table 4.4. Results of some coefficients are very similar while other differ significantly. These large uncertainties emerging from the database difference need to be accounted for. For better evaluation of these uncertainties, additional methods can be used [26] [27].

Table 4.4: Multiplication coefficients for TRINITY database in relation to Morgan database.

| Coefficient name | Multiplication factor |
|---|---|
| Rate coeff. a) | 1,9 |
| Rate coeff. b) | 0,78 |
| Rate coeff. d) | 1,55 |
| Rate coeff. e) | 7 |
| Rate coeff. f) | 0,91 |
| Mean energy | 0,97 |
| Ionization freq. | 0,96 |
| Attachment freq. | 0,85 |
| Ionization coeff. | 1 |
| Attachment coeff. | 0,85 |

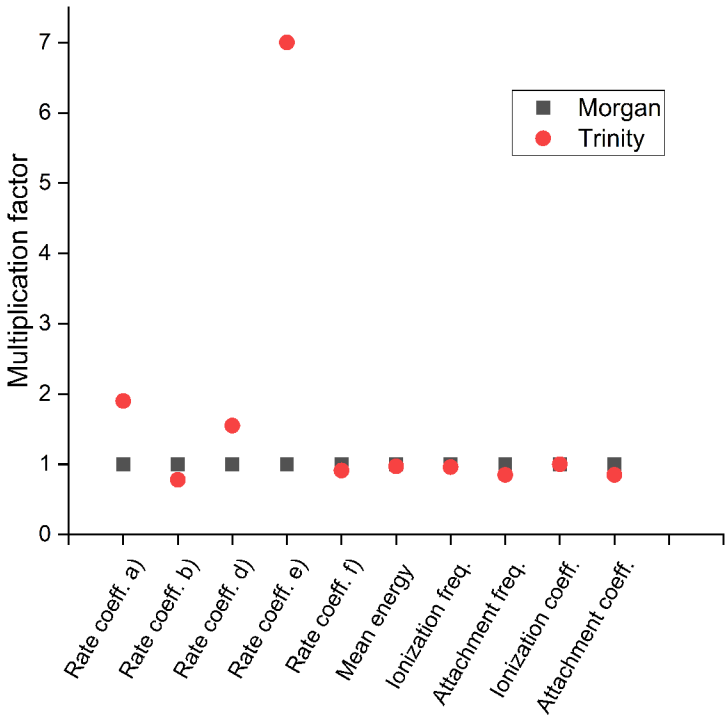


Figure 4.14: Comparison of results from used databases. Letters near rate coefficients denote their belonging to certain reaction in fig. 4.13. Rate coefficient c) is only available in Trinity database and is therefore not shown in this figure.

# 5 Conclusion and outlook

In this thesis, triple junction on surface barrier discharge was examined. Theory related to this issue was widely discussed. It included basic properties of DBDs, description of measuring methods and derivation of used equations from equivalent circuit models.

Experiment with tube of fused silica partially submerged in water was examined. Resulting Q-V plots were very different from what equivalent circuit model would expect. We attribute observed Q-V plot profile to charge transfer in water, which served as dielectric barrier. Because ions have much lower mobility than electrons, charge transfer probably continued after discharging in gas gap stopped. This is supported by observable phase delay of voltage behind transferred charge function. This effect created too big uncertainties in capacitances to be analyzed.

Experiment with humid air in setup of parallel plates was examined. Q-V plots with not-ideal parallelogram shape were observed. Compliant to equivalent model, capacitances $C_d$ and $C_{cell}$ were determined. Different discharge developments were observed for different voltage polarities, as we would expect from asymmetric experimental setup (in terms of DB coverage). Discharge current and transferred charge were calculated; electric field of the streamer head estimated at the point when it was situated near the triple junction.

Unfortunately, we did not manage to obtain a good estimate of electric field; it was lower than what one would expect based on known measurements of similar discharges. We intent to improve this approach. Most importantly, to use alternative equivalent circuit model by estimating $\alpha$ and $\beta$ coefficients. Experiment would need to be modified so that the covered electrode would coincide with the discharge area. Electrode capacitance could also be measured in suitable setup. It would also be convenient to seek for discharge modes/configurations where triple junction with water could be examined. Neutral density was calculated considering ideal gas. More realistic equation of state could be used.

Chosen rate and transfer coefficients were calculated with the BOLSIG+ software. Two cross-section databases were compared. It turned out that differencies between databases are signifficant, one thus has to consider ade-

quate database for his cause. It is possible to use some kind of method of uncertainty evaluation, e.g. [26] [27].

# Bibliography


1. KULIKOVSKY, A. A. Positive streamer in a weak field in air: A moving avalanche-to-streamer transition. *Phys. Rev. E*. 1998, vol. 57, pp. 7066–7074. Available from DOI: 10.1103/PhysRevE.57.7066.
2. PAVLINAK, David; GALMIZ, O; ZEMÁNEK, Miroslav; BRABLEC, A; ČECH, Jan; ČERNÁK, Mirko. Permanent hydrophilization of outer and inner surfaces of polytetrafluoroethylene tubes using ambient air plasma generated by surface dielectric barrier discharges. *Applied Physics Letters*. 2014, vol. 105, pp. 154102. Available from DOI: 10.1063/1.4898134.
3. TULLY, L.K.; WHITE, A.D.; GOERZ, David; JAVEDANI, Jalal; HOUCK, T.L. Electrostatic Modeling of Vacuum Insulator Triple Junctions. In: 2007, vol. 2, pp. 1195–1200. Available from DOI: 10.1109/PPPS.2007.4652401.
4. BRANDENBURG, Ronny. Dielectric barrier discharges: progress on plasma sources and on the understanding of regimes and single filaments. *Plasma Sources Science and Technology*. 2017, vol. 26, no. 5, pp. 053001. Available from DOI: 10.1088/1361-6595/aa6426.
5. SIEMENS, W. Ueber die elektrostatische Induction und die Verzögerung des Stroms in Flaschendrähten. *Annalen der Physik*. 1857, vol. 178, no. 9, pp. 66–122. Available from DOI: 10.1002/andp.18571780905.
6. ČECH, Jan; HANUSOVÁ, Jana; SŤAHEL, Pavel; ČERNÁK, Mirko. Diffuse Coplanar Surface Barrier Discharge in Artificial Air: Statistical Behaviour of Microdischarges. *Open Chemistry*. 2015, vol. 13. ISSN 2391-5420. Available from DOI: http://dx.doi.org/10.1515/chem-2015-0062.
7. WAGNER, H.-E.; BRANDENBURG, R.; KOZLOV, K.V.; SONNENFELD, A.; MICHEL, P.; BEHNKE, J.F. The barrier discharge: basic properties and applications to surface treatment. *Vacuum*. 2003, vol. 71, no. 3, pp. 417–436. ISSN 0042-207X. Available from DOI: https://doi.org/10.1016/S0042-207X(02)00765-0. Symposium on Plasma Surface Engineering at the Spring Meeting of the German Physical Society, Regensburg, Germany, March 11-15 2002.
8. RAIZER, Yuri P. *Gas discharge physics*. Springer, 1991. ISBN 3-540-19462-2.

9. BRUGGEMAN, Peter J; IZA, Felipe; BRANDENBURG, Ronny. Foundations of atmospheric pressure non-equilibrium plasmas. *Plasma Sources Science and Technology*. 2017, vol. 26, no. 12, pp. 123002. Available from DOI: 10.1088/1361-6595/aa97af.

10. GIBALOV, Valentin I; PIETSCH, Gerhard J. Dynamics of dielectric barrier discharges in different arrangements. *Plasma Sources Science and Technology*. 2012, vol. 21, no. 2, pp. 024010. Available from DOI: 10.1088/0963-0252/21/2/024010.

11. GIBALOV, Valentin I; PIETSCH, Gerhard J. The development of dielectric barrier discharges in gas gaps and on surfaces. *Journal of Physics D: Applied Physics*. 2000, vol. 33, no. 20, pp. 2618–2636. Available from DOI: 10.1088/0022-3727/33/20/315.

12. LAGMICH, Y; CALLEGARI, Th; PITCHFORD, L C; BOEUF, J P. Model description of surface dielectric barrier discharges for flow control. *Journal of Physics D: Applied Physics*. 2008, vol. 41, no. 9, pp. 095205. Available from DOI: 10.1088/0022-3727/41/9/095205.

13. GROSCH, H.; HODER, T.; WELTMANN, K.-D.; BRANDENBURG, R. Spatio-temporal development of microdischarges in a surface barrier discharge arrangement in air at atmospheric pressure. *Eur. Phys. J. D*. 2010, vol. 60, no. 3, pp. 547–553. Available from DOI: 10.1140/epjd/e2010-00239-8.

14. KOZLOV, K V; WAGNER, H-E; BRANDENBURG, R; MICHEL, P. Spatio-temporally resolved spectroscopic diagnostics of the barrier discharge in air at atmospheric pressure. *Journal of Physics D: Applied Physics*. 2001, vol. 34, no. 21, pp. 3164–3176. Available from DOI: 10.1088/0022-3727/34/21/309.

15. PIPA, A. V.; KOSKULICS, J.; BRANDENBURG, R.; HODER, T. The simplest equivalent circuit of a pulsed dielectric barrier discharge and the determination of the gas gap charge transfer. *Review of Scientific Instruments*. 2012, vol. 83, no. 11, pp. 115112. Available from DOI: 10.1063/1.4767637.

16. PIPA, A. V.; HODER, T.; KOSKULICS, J.; SCHMIDT, M.; BRANDENBURG, R. Experimental determination of dielectric barrier discharge capacitance. *Review of Scientific Instruments*. 2012, vol. 83, no. 7, pp. 075111. Available from DOI: 10.1063/1.4737623.

17. PEETERS, F J J; SANDEN, M C M van de. The influence of partial surface discharging on the electrical characterization of DBDs. *Plasma Sources Science and Technology*. 2014, vol. 24, no. 1, pp. 015016. Available from DOI: 10.1088/0963-0252/24/1/015016.

18. HAGELAAR, G J M; PITCHFORD, L C. Solving the Boltzmann equation to obtain electron transport coefficients and rate coefficients for fluid models. *Plasma Sources Science and Technology*. 2005, vol. 14, no. 4, pp. 722–733. Available from DOI: 10.1088/0963-0252/14/4/011.

19. PAI, David Z; STAUSS, Sven; TERASHIMA, Kazuo. Field-emitting Townsend regime of surface dielectric barrier discharges emerging at high pressure up to supercritical conditions. *Plasma Sources Science and Technology*. 2015, vol. 24, no. 2, pp. 025021. Available from DOI: 10.1088/0963-0252/24/2/025021.

20. KRIEGSEIS, Jochen; MÖLLER, Benjamin; GRUNDMANN, Sven; TROPEA, Cameron. Capacitance and power consumption quantification of dielectric barrier discharge (DBD) plasma actuators. *Journal of Electrostatics - J ELECTROSTAT*. 2011, vol. 69, pp. 302–312. Available from DOI: 10.1016/j.elstat.2011.04.007.

21. BABAEVA, Natalia Yu; TERESHONOK, Dmitry V; NAIDIS, George V. Fluid and hybrid modeling of nanosecond surface discharges: effect of polarity and secondary electrons emission. *Plasma Sources Science and Technology*. 2016, vol. 25, no. 4, pp. 044008. Available from DOI: 10.1088/0963-0252/25/4/044008.

22. HODER, T; SYNEK, P; CHORVÁT, D; RÁHEL', J; BRANDENBURG, R; ČERNÁK, M. Complex interaction of subsequent surface streamers via deposited charge: a high-resolution experimental study. *Plasma Physics and Controlled Fusion*. 2017, vol. 59, no. 7, pp. 074001. Available from DOI: 10.1088/1361-6587/aa6ea2.

23. BRANDENBURG, Ronny et al. White paper on the future of plasma science in environment, for gas conversion and agriculture. *Plasma Processes and Polymers*. 2019, vol. 16, no. 1, pp. 1700238. Available from DOI: 10.1002/ppap.201700238.

24. Morgan and TRINITY databases, www.lxcat.net, retrieved on 9th of April 2019.

25. PITCHFORD, Leanne C. et al. LXCat: an Open-Access, Web-Based Platform for Data Needed for Modeling Low Temperature Plasmas. *Plasma Processes and Polymers*. 2017, vol. 14, no. 1-2, pp. 1600098. Available from DOI: 10.1002/ppap.201600098.

26. OBRUSNÍK, Adam; BÍLEK, Petr; HODER, Tomáš; ŠIMEK, Milan; BONAVENTURA, Zdeněk. Electric field determination in air plasmas from intensity ratio of nitrogen spectral bands: I. Sensitivity analysis and uncertainty quantification of dominant processes. *Plasma Sources Science and Technology*. 2018, vol. 27, no. 8, pp. 085013. Available from DOI: 10.1088/1361-6595/aad663.

27. BÍLEK, Petr; OBRUSNÍK, Adam; HODER, Tomáš; ŠIMEK, Milan; BONAVENTURA, Zdeněk. Electric field determination in air plasmas from intensity ratio of nitrogen spectral bands: II. Reduction of the uncertainty and state-of-the-art model. *Plasma Sources Science and Technology*. 2018, vol. 27, no. 8, pp. 085012. Available from DOI: 10.1088/1361-6595/aad666.